



SN2019dge: A Helium-rich Ultra-stripped Envelope Supernova

Yuhan Yao¹, Kishalay De¹, Mansi M. Kasliwal¹, Anna Y. Q. Ho¹, Steve Schulze², Zhihui Li¹, S. R. Kulkarni¹, Andrew Fruchter³, David Rubin^{3,4}, Daniel A. Perley⁵, Jim Fuller⁶, Anthony L. Piro⁷, C. Fremling⁸, Eric C. Bellm⁹, Rick Burruss¹⁰, Dmitry A. Duev⁸, Michael Feeney¹⁰, Avishay Gal-Yam², V. Zach Golkhou^{9,11}, Matthew J. Graham⁸, George Helou¹², Thomas Kupfer¹³, Russ R. Laher¹², Frank J. Masci¹², Adam A. Miller^{14,15}, Ben Rusholme¹², David L. Shupe¹², Roger Smith¹⁰, Jesper Sollerman¹⁶, Maayane T. Soumagnac^{2,17}, and Jeffry Zolkower¹⁰

¹ Cahill Center for Astrophysics, California Institute of Technology, MC 249-17, 1200 E California Boulevard, Pasadena, CA 91125, USA; yyao@astro.caltech.edu

² Department of Particle Physics and Astrophysics, Weizmann Institute of Science, 234 Herzl Street, 76100 Rehovot, Israel

³ Space Telescope Science Institute, 3700 San Martin Drive, Baltimore, MD 21218, USA

⁴ Department of Physics and Astronomy, University of Hawai'i, 2680 Woodlawn Drive, Honolulu, HI 96822, USA

⁵ Astrophysics Research Institute, Liverpool John Moores University, IC2, Liverpool Science Park, 146 Brownlow Hill, Liverpool L3 5RF, UK

⁶ TAPIR, California Institute of Technology, MC 350-17, 1200 E California Boulevard, Pasadena, CA 91125, USA

⁷ The Observatories of the Carnegie Institution for Science, 813 Santa Barbara Street, Pasadena, CA 91101, USA

⁸ Division of Physics, Mathematics, and Astronomy, California Institute of Technology, Pasadena, CA 91125, USA

⁹ DIRAC Institute, Department of Astronomy, University of Washington, 3910 15th Avenue NE, Seattle, WA 98195, USA

¹⁰ Caltech Optical Observatories, California Institute of Technology, Pasadena, CA 91125, USA

¹¹ The eScience Institute, University of Washington, Seattle, WA 98195, USA

¹² IPAC, California Institute of Technology, 1200 E. California Boulevard, Pasadena, CA 91125, USA

¹³ Kavli Institute for Theoretical Physics, University of California, Santa Barbara, CA 93106, USA

¹⁴ Center for Interdisciplinary Exploration and Research in Astrophysics (CIERA) and Department of Physics and Astronomy, Northwestern University, 1800 Sherman Road, Evanston, IL 60201, USA

¹⁵ The Adler Planetarium, Chicago, IL 60605, USA

¹⁶ The Oskar Klein Centre, Department of Astronomy, Stockholm University, AlbaNova, SE-10691 Stockholm, Sweden

¹⁷ Lawrence Berkeley National Laboratory, 1 Cyclotron Road, Berkeley, CA 94720, USA

Received 2020 May 27; revised 2020 July 23; accepted 2020 July 27; published 2020 August 31

Abstract

We present observations of ZTF18abfcmjw (SN2019dge), a helium-rich supernova with a fast-evolving light curve indicating an extremely low ejecta mass ($\approx 0.33 M_{\odot}$) and low kinetic energy ($\approx 1.3 \times 10^{50}$ erg). Early-time (< 4 days after explosion) photometry reveals evidence of shock cooling from an extended helium-rich envelope of $\sim 0.1 M_{\odot}$ located $\sim 1.2 \times 10^{13}$ cm from the progenitor. Early-time He II line emission and subsequent spectra show signatures of interaction with helium-rich circumstellar material, which extends from $\gtrsim 5 \times 10^{13}$ cm to $\gtrsim 2 \times 10^{16}$ cm. We interpret SN2019dge as a helium-rich supernova from an ultra-stripped progenitor, which originates from a close binary system consisting of a mass-losing helium star and a low-mass main-sequence star or a compact object (i.e., a white dwarf, a neutron star, or a black hole). We infer that the local volumetric birth rate of 19dge-like ultra-stripped SNe is in the range of $1400\text{--}8200 \text{ Gpc}^{-3} \text{ yr}^{-1}$ (i.e., 2%–12% of core-collapse supernova rate). This can be compared to the observed coalescence rate of compact neutron star binaries that are not formed by dynamical capture.

Unified Astronomy Thesaurus concepts: [Supernovae \(1668\)](#); [Core-collapse supernovae \(304\)](#); [Neutron stars \(1108\)](#); [Surveys \(1671\)](#)

Supporting material: machine-readable table

1. Introduction

Type Ibc supernovae (SNe Ibc) are believed to be explosions of massive stars that have lost their hydrogen envelopes (Filippenko 1997; Gal-Yam 2017). Their typical rise times (t_{rise} in the range of 10–25 days) and peak luminosities ($M_{R,\text{peak}}$ between -17 and -19 mag) suggest ejecta masses (M_{ej}) of $1\text{--}5 M_{\odot}$ and ^{56}Ni masses (M_{Ni}) of $0.1\text{--}0.4 M_{\odot}$ (Drout et al. 2011; Taddia et al. 2018; Prentice et al. 2019). The relatively low M_{ej} and high rates of SNe Ibc are not compatible with predictions from the evolution of single massive stars, whose mass-loss rates are not high enough to strip most of the outer layers (Smith et al. 2011; Lyman et al. 2016). In contrast, Wolf-Rayet (WR) or helium star descendants of massive stars in close binary systems are thought to be the dominant progenitors for the SNe Ibc population (Dessart et al. 2012; Eldridge et al. 2013).

SNe Ibc with the lowest M_{ej} arise from core-collapse of a stellar core with a small envelope. This can occur in tight

binaries in which a helium star transfers mass to a companion that is small in size. Such a scenario was invoked by Nomoto et al. (1994) as one way to explain the fast evolution of the Type Ic SN1994I with a carbon-oxygen progenitor star of $\sim 2 M_{\odot}$ and $M_{\text{ej}} \sim 0.9 M_{\odot}$. Should the degree of stripping be even more extreme, we may expect the so-called ultra-stripped envelope SNe, in which M_{ej} and M_{Ni} are on the order of $0.1 M_{\odot}$ and $0.01 M_{\odot}$, respectively (Tauris et al. 2013, 2015; Suwa et al. 2015). These weak explosions are one of the two channels to form double neutron star (DNS) binaries that are compact enough to merge within a *Hubble* time because of gravitational wave (GW) radiation (Piran & Shaviv 2005; Beniamini & Piran 2016; Tauris et al. 2017).¹⁸ Ultra-stripped SNe are therefore a promising progenitor channel of multi-messenger sources that can be jointly studied

¹⁸ The other channel to form compact DNSs is dynamical capture in a dense stellar environment, such as a globular cluster (East & Pretorius 2012; Andrews & Mandel 2019).

by the LIGO/VIRGO network and electromagnetic efforts (Abbott et al. 2017a, 2017b; Coulter et al. 2017; Goldstein et al. 2017; Hallinan et al. 2017; Kasliwal et al. 2017).

Compared with canonical SNe Ibc, we expect light curves of ultra-stripped SNe to be rapidly evolving and subluminous due to the small amount of M_{ej} and M_{Ni} produced. Among the group of faint and fast objects, SN2005ek (Drout et al. 2013), SN2010X (Kasliwal et al. 2010), as well as some of the calcium-rich gap transients including PTF10iuv (Kasliwal et al. 2012), iPTF16hgs (De et al. 2018b), and SN2019ehk (Jacobson-Galán et al. 2020; Nakaoka et al. 2020) have been suggested as good candidates for ultra-stripped SNe (Moriya et al. 2017). However, properties of these objects are also consistent with alternative interpretations, including core-collapse of stars with extended hydrogen-free envelopes (Kleiser & Kasen 2014; Kleiser et al. 2018a, 2018b), and explosive detonation of a helium shell on the surface of white dwarfs (Shen et al. 2010; Sim et al. 2012; Jacobson-Galán et al. 2019; Polin et al. 2019; De et al. 2020a).

The most convincing ultra-stripped event to date is the Type Ic SN iPTF14gqr (De et al. 2018c). Its radioactivity-powered emission reveals $M_{\text{ej}} \sim 0.2 M_{\odot}$ and $M_{\text{Ni}} \sim 0.05 M_{\odot}$, whereas the detection of early-time shock cooling signatures shows that the progenitor is an extended massive star instead of a white dwarf, and therefore pins down its core-collapse origin. Discovered within one day of explosion, iPTF14gqr also demonstrated the importance of early-time observations in securely identifying ultra-stripped SNe.

Here we report the discovery, observations, and modeling of the rapidly rising ($t_{\text{rise}} \lesssim 3$ days) subluminous ($M_{r,\text{peak}} \sim -16.3$ mag) helium-rich event ZTF18abfcmjw (SN2019dge) discovered by the Zwicky Transient Facility (ZTF; Bellm et al. 2019b; Graham et al. 2019). SN2019dge is consistent with being a helium-rich ultra-stripped SN. Section 2 describes the discovery and follow-up observations. Section 3 outlines the basic properties of the explosion and its host galaxy. Section 4 shows modeling of this transient. Section 5 provides a discussion on the progenitor system, and Section 6 presents the estimated volumetric rates of 19dge-like ultra-stripped SNe. Section 7 gives a conclusion of this paper. Calculations in this paper assume a Λ CDM cosmology with $H_0 = 70 \text{ km s}^{-1} \text{ Mpc}^{-1}$, $\Omega_m = 0.27$, and $\Omega_{\Lambda} = 0.73$ (Komatsu et al. 2011). All spectra and photometry will be made available by the WISeREP repository (Yaron & Gal-Yam 2012) following publication.

2. Observations

2.1. Discovery

SN2019dge was discovered by ZTF, which runs on the Palomar Oschin Schmidt 48-inch (P48) telescope (Dekany et al. 2020). The first real-time alert (Patterson et al. 2019) was generated on 2019 April 7 10:18:46 (JD = 2458580.9297) for a g -band detection at 20.66 ± 0.34 mag and J2000 coordinates $\alpha = 17^{\text{h}}36^{\text{m}}46^{\text{s}}.75$, $\delta = +50^{\circ}32^{\text{m}}52^{\text{s}}.2$. On April 8, a new alert was flagged by a science program filter on the GROWTH Marshal (Kasliwal et al. 2019), which is designed to look for fast-evolving transients (Ho et al. 2020a).

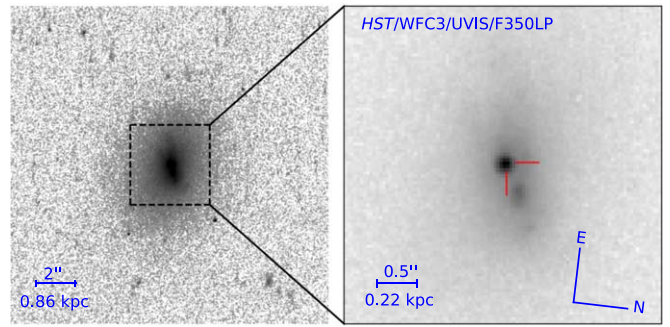


Figure 1. HST image of the field on April 22 in the F350LP filter at two intensity scales. The position of SN2019dge is marked by the red crosshairs in the right panel.

2.2. Follow-up Observations

2.2.1. HST Observation

Hubble Space Telescope (HST) observations were obtained as part of our HST “Rolling Snapshots” pilot experiment (GO-15675). This new observational approach requires the PI to update a list of objects of interest each week before the schedule is built, giving the scheduler flexibility to choose a possible source for snapshots. Under this program, we obtained a NUV spectrum using the WFC3 G280 grism, a short (60 s) direct image of this field in the F300X filter to set the wavelength scale of the spectrum, as well as a longer exposure (200 s) in the F350LP filter. The image in the F350LP filter is shown in Figure 1. It has very similar throughput to the zeroth order of the G280 grism.

SN2019dge resides in a compact galaxy SDSS J173646.73+503252.3. From our follow-up spectra (see Section 3.2), we measure a host redshift of $z = 0.0213$, corresponding to a luminosity distance of $D_L = 93$ Mpc. Figure 1 shows that there is a surface brightness peak to the northwest of SN2019dge (~ 0.2 kpc away), which might trace a star-forming region. A thorough analysis of the host-galaxy properties is given in Appendix C.

2.2.2. Optical Photometry

Following Yao et al. (2019), we perform forced point-spread function (PSF) photometry on ZTF difference images generated with the ZTF real-time reduction and image subtraction pipeline (Masci et al. 2019). ZTF image subtraction is based on the Zackay et al. (2016) image subtraction method. The sky region of SN2019dge is covered by two ZTF fields with “fieldid” (i.e., ZTF field identifier) 763 and 1799. We exclude all data in field 1799 because the reference image was constructed using images obtained between 2018 May 25 and 2019 July 12, which is after the explosion of the transient. Although the ZTF name of this object (ZTF18abfcmjw) may indicate that the transient was discovered in 2018, this is due to an alert generated on 2018 July 7 from a candidate detection in negative subtraction (reference minus science) in field 763. We note that the seeing during that night was $4''.2$, larger than 99% of Palomar nights. The irregularly shaped PSF might cause over-subtraction around the galaxy nucleus in the difference imaging process.

Because field 763 was included in both the Northern Sky Survey with two epochs (one epoch each in g and r) per three nights and the extragalactic high-cadence survey with six

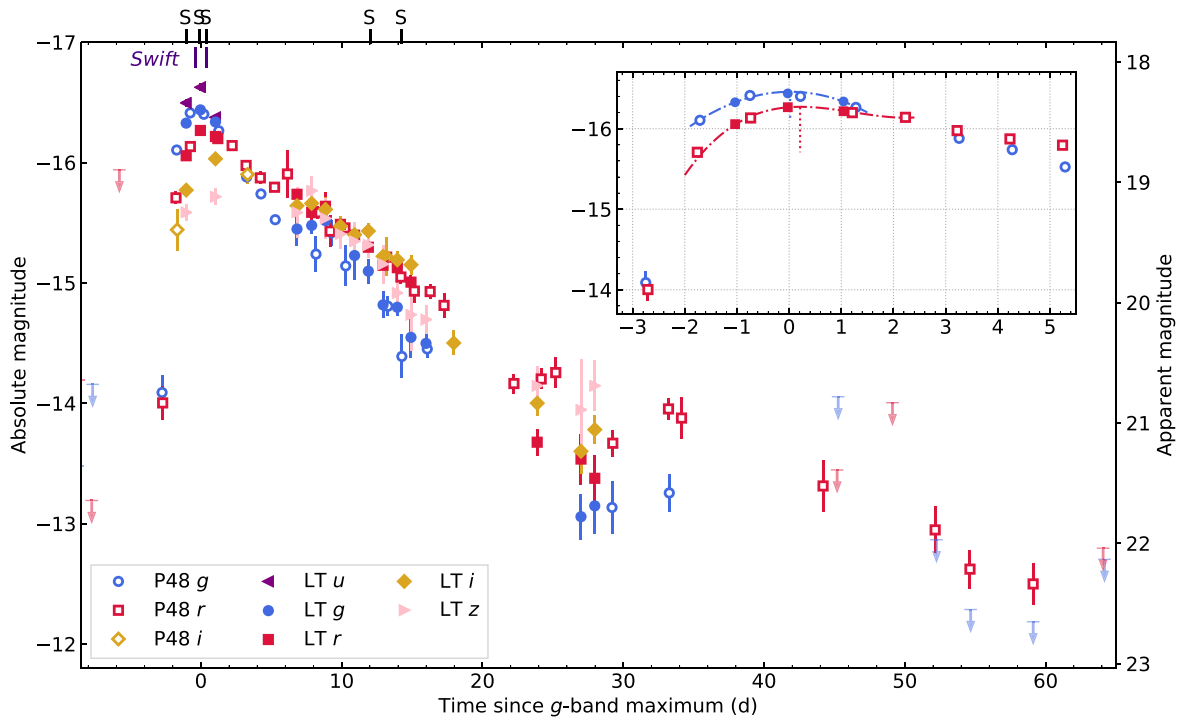


Figure 2. Galactic extinction corrected optical light curve of SN2019dge. The inset shows the light curve in g and r bands zoomed around the region of maximum light. Along the upper axis, epochs of spectroscopy are marked with the letter S above the axis, while two epochs of Swift/UVOT/XRT observations are marked below the axis.

epochs (three epochs each in g and r) per night (see Bellm et al. 2019a for the design of ZTF experiments), SN2019dge is visited multiple times every night. Therefore, single-night flux measurements in the same filter are binned (by taking the inverse variance-weighted average). This gives a pre-explosion r -band limit of 18.95 mag (5σ limit computed at the expected position of the transient) on April 4 10:36:34. We convert 5σ detections to AB magnitudes for further analysis.

Following the discovery of SN2019dge, we obtain follow-up photometry in $ugriz$ with an optical imager (IO:O) on the Liverpool Telescope (LT; Steele et al. 2004). Digital image subtraction and photometry for LT imaging is performed using the Fremling Automated Pipeline (FPipe; Fremling et al. 2016). Fpipe performs calibration and host subtraction against Sloan Digital Sky Survey reference images and catalogs (SDSS, Alam et al. 2015).

LT and P48 photometry are shown in Figure 2. Absolute and apparent magnitudes are corrected for Galactic extinction $E(B - V) = 0.022$ mag (Schlafly & Finkbeiner 2011). We assume $R_V = 3.1$, and adopt the reddening law from Cardelli et al. (1989). We do not correct for host-galaxy contamination given the absence of Na I D absorption in all spectra at the host redshift. To estimate the epoch of maximum light, we interpolate the g - and r -band photometry with three-order polynomial functions, as shown in the inset of Figure 2. The time window used in the fit is from MJD = 58581.2 to 58585.2. SN2019dge is found to peak at $M_{g,\text{peak}} = -16.45 \pm 0.03$ mag on MJD = 58583.19, and $M_{r,\text{peak}} = -16.27 \pm 0.02$ mag on MJD = 58583.39. Hereafter we use phase (Δt) to denote time with respect to the g -band maximum light epoch, MJD = 58583.2.

We obtain one epoch of late-time imaging with the Wafer Scale Imager for Prime (WASP) mounted on the Palomar 200-inch telescope at $\Delta t \approx 85$ d. The data are obtained in r band with a total exposure time of 900 s divided into dithered

exposures of 300 s each. The data are reduced using standard techniques as described in De et al. (2020a). Image subtraction is performed using archival reference images from the Dark Energy Legacy Survey (Dey et al. 2019), using the method described in De et al. (2020a). The median 5σ limiting magnitude of the image is $r \approx 25$ mag. However, the depth at the transient location is limited by the noise from the bright host galaxy, and the transient is not detected to a 5σ limiting magnitude of $r = 22.1$ mag.

We also perform forced photometry on archival PTF/iPTF difference images spanning 2009 May 7–2016 June 13 (Law et al. 2009; Rau et al. 2009). No historical detection is found.

2.2.3. Swift Observation

Observations with the Neil Gehrels Swift Observatory (Swift; Gehrels et al. 2004) was triggered on April 9 and April 10. Ultraviolet/Optical Telescope (UVOT; Roming et al. 2005) data were obtained in the $UVW1$, $UVM2$, $UVW2$, U , B , and V filters.

UVOT data are reduced using HEASOFT (HEASARC 2014) version 6.17 with a $3''$ circular aperture. To remove host-galaxy contribution at the location of the SN, we obtained a final epoch in all broadband filters on 2019 June 23 and measured the photometry with the same aperture used for the transient. We present a table of our optical and UV photometry in Appendix A.

In parallel with the UVOT observations, Swift observed SN2019dge with its X-ray telescope (XRT; Burrows et al. 2005) between 0.3 and 10 keV in the photon counting mode. We note that no point sources were detected in the XRT event files with $\text{SNR} > 3$. The 3σ limits (in count s^{-1}) in the April 9, April 10, and June 23 observations are 7.8×10^{-3} , 5.8×10^{-3} , and 6.1×10^{-3} , respectively. To convert the upper limit count-rate to flux, we adopt the Galactic neutral-

Table 1
Log of SN2019dge Spectroscopy

Start Time (UTC)	Instrument	Phase (day)	Exposure Time (s)	Airmass	Resolution (FWHM) (Å)
2019 Apr 9 03:30:28	LT + SPRAT	−1.1	500	1.80	18
2019 Apr 10 03:06:10	LT + SPRAT	−0.1	500	1.80	18
2019 Apr 10 14:21:44	Keck I + LRIS	+0.4	300	1.17	6
2019 Apr 22 05:08:00	HST + WFC3 + UVIS	+12.0	2×250	...	43
2019 Apr 24 11:06:43	P200 + DBSP	+14.3	1200	1.05	3–5
2019 Jul 4 11:49:18	Keck I + LRIS	+85.3	1740	1.42	6
2019 Aug 31 08:04:58	Keck I + LRIS	+143.1	1150	1.41	6
2019 Sep 28 08:14:27	Keck I + LRIS	+171.1	600	2.17	6
2020 Feb 18 15:23:40	Keck I + LRIS	+314.4	1450	1.38	6

Note. Phase is measured relative to g -band maximum (MJD = 58583.2).

hydrogen column density of $N_{\text{H}} = 2.89 \times 10^{20} \text{ cm}^{-2}$ toward SN2019dge (Willingale et al. 2013) and a power-law spectrum in the form of $N(E) \propto E^{-1}$, where $N(E)$ has the unit of photons $\text{cm}^{-2} \text{ s}^{-1} \text{ keV}^{-1}$. Using the PIMMS web tool,¹⁹ we obtain unabsorbed flux upper limits in the 0.3–10 keV band of 5.22, 3.88, and $4.08 \times 10^{-13} \text{ erg s}^{-1} \text{ cm}^{-2}$, corresponding to luminosities of 5.37, 4.00, and $4.20 \times 10^{41} \text{ erg s}^{-1}$. We note that these limits are shallower than X-ray luminosities expected to be seen in SNe (Ofek et al. 2013a).

2.2.4. Radio Follow-up

Shortly after the discovery of SN2019dge, we initiate radio follow-up observations in order to constrain the presence of a radio counterpart, as potentially expected in some rapid-rising transients with circumstellar interaction (Weiler et al. 2007; Horesh et al. 2013; Ho et al. 2019b). We observed at high-frequency radio bands using the Submillimeter Array (SMA, Ho et al. 2004) on UT 2019 April 9 between 15:49:17 and 19:51:26 under its target-of-opportunity program. The project ID is 2018B-S047 (PI: Anna Ho). We did not detect SN2019dge in the resulting image, and the 3σ upper limits are 2.25 mJy at 230 GHz and 8.4 mJy at 345 GHz.

2.2.5. Spectroscopy

We obtain eight optical spectroscopic follow-up observations of SN2019dge from −1.1 days to +314.4 days relative to g -band peak using the Spectrograph for Rapid Acquisition of Transients (SPRAT; Piascik et al. 2014) on the LT, the Double Spectrograph (DBSP) on the 200-inch Hale telescope (Oke & Gunn 1982), and the Low Resolution Imaging Spectrograph (LRIS) on the Keck I telescope (Oke et al. 1995). To extract the LT spectra, we use the automated SPRAT reduction pipeline, which is a modification of the pipeline for FrodoSpec (Barnsley et al. 2012). The DBSP spectrum is reduced using a PyRAF-based reduction pipeline (Bellm & Sesar 2016). LRIS spectra are reduced and extracted using Lpipe (Perley 2019).

A log of our spectroscopic observations is given in Table 1. We present our sequence of spectra in Figures 6, 7, and 10.

3. Properties of the Explosion

3.1. Light-curve Properties

3.1.1. Peak Luminosity and Rise and Decline Timescales

The g - and r -band peak luminosity of SN2019dge (≈ -16.3 mag) is around the lower limit of stripped envelope SNe (Drout et al. 2011; Taddia et al. 2018; Prentice et al. 2019), and akin to those of the Ca-rich gap transients, which occupy the luminosity “gap” between novae and SNe (peak absolute magnitude $M_R \approx -15.5$ to -16.5 mag, Kasliwal et al. 2012).

To characterize the rise and decline timescales of SN2019dge, following Ho et al. (2020b), we calculate rise time (t_{rise}) defined by how long it takes the r -band light curve to rise from 0.75 mag below peak to peak, and decline time (t_{decay}) determined by how long it takes to decline from peak by 0.75 mag (corresponding to half of maximum flux). Because SN2019dge shows no evidence of hydrogen (Section 3.2) and exhibits a fast rise (Figure 2), we compare the t_{rise} , t_{decay} , and peak absolute magnitude between SN2019dge and two other groups of transients:

1. Fast-evolving hydrogen-deficient transients that are fainter than normal SNe Ia (i.e., < -19 mag), including SN2002bj (Poznanski et al. 2010), SN2005ek (Drout et al. 2013), PTF09dav (Sullivan et al. 2011), SN2010X (Kasliwal et al. 2010), PTF10iuv (Kasliwal et al. 2012), iPTF14gqr (De et al. 2018c), iPTF16hgs (De et al. 2018b), SN2018kzr (McBrien et al. 2019), and SN2019bkc (Chen et al. 2020).
2. “Fast-evolving luminous transients” (FELT, Rest et al. 2018) or “fast blue optical transients” (FBOT, Margutti et al. 2019). We select well-studied representative objects of this population, including KSN2015K (Rest et al. 2018), iPTF16asu (Whitesides et al. 2017), AT2018cow (Prentice et al. 2018; Perley et al. 2019), SN2018gep (Ho et al. 2019a), and ZTF18abvkwla (also known as the Koala; Ho et al. 2020b).

In Figure 3, peak magnitudes are given in (observer-frame) r band, except for KSN2015K, for which we only have observations in the Kepler “white” filter, and iPTF16asu, for which the rise was caught only in g band. We correct only for Galactic extinction to compute $M_{r,\text{peak}}$ (assuming no host extinction). Note that iPTF14gqr and iPTF16hgs are SNe exhibiting double-peaked light curves. Because the rise to first peak was not captured, an upper limit of t_{rise} is calculated by taking the time difference between the first r -band detection

¹⁹ <https://heasarc.gsfc.nasa.gov/cgi-bin/Tools/w3pimms/w3pimms.pl>

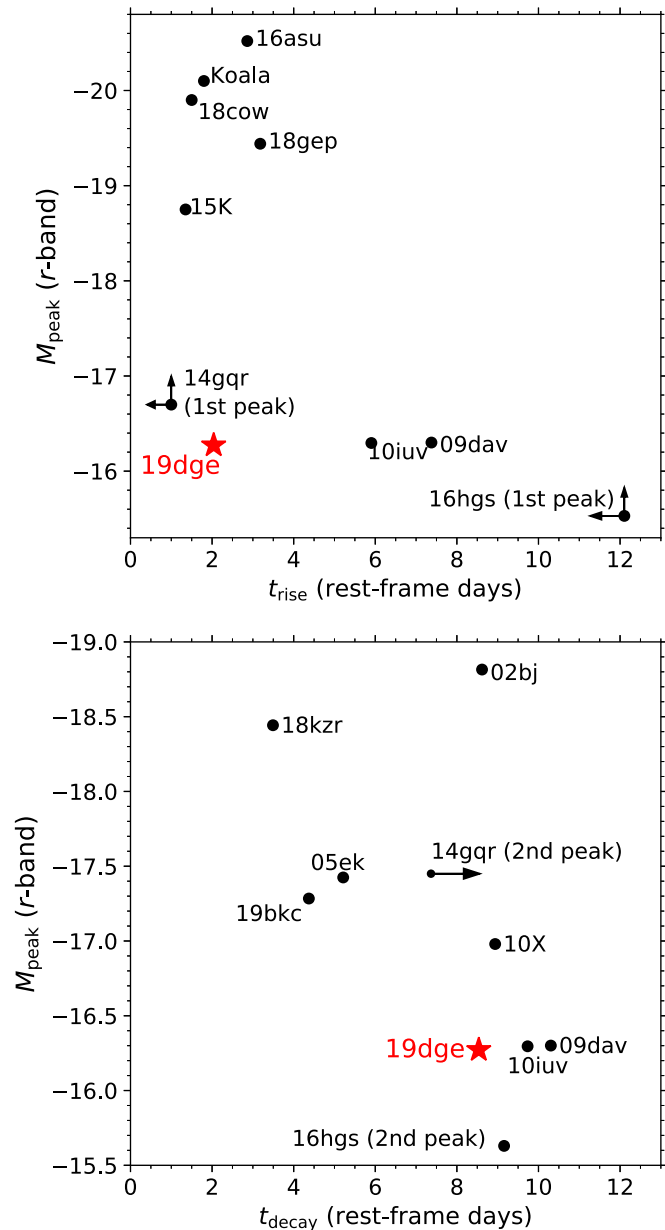


Figure 3. Comparison of the photometric evolution timescales (t_{rise} and t_{decay}) and r -band peak absolute magnitudes of SN2019dge (red asterisks) with other fast-evolving transients (black dots). See the text for details.

and the latest pre-discovery nondetection,²⁰ and absolute magnitude of the first r -band detection is considered to be a fainter limit of $M_{r,\text{peak}}$ (plotted in the upper panel). In the lower panel, because observations of iPTF14gqr do not extend to 0.75 mag below its second peak, we present a lower limit of its t_{decay} .

It is clear from the upper panel of Figure 3 that SN2019dge rose faster than normal Ca-rich events, such as PTF09dav and PTF10iuv. The t_{rise} of ≈ 2.0 days is similar to the population of FELTs/FBOTs, but SN2019dge is substantially fainter. In the subluminous regime, iPTF14gqr has t_{rise} comparable to SN2019dge, and its first peak has been postulated to be caused by the diffusion of shock-deposited energy out of an envelope around the progenitor star (De et al. 2018c).

²⁰ For the second peak, $t_{\text{rise}} \sim 5$ days for iPTF14gqr and $8 < t_{\text{rise}} < 20$ days for iPTF16hgs.

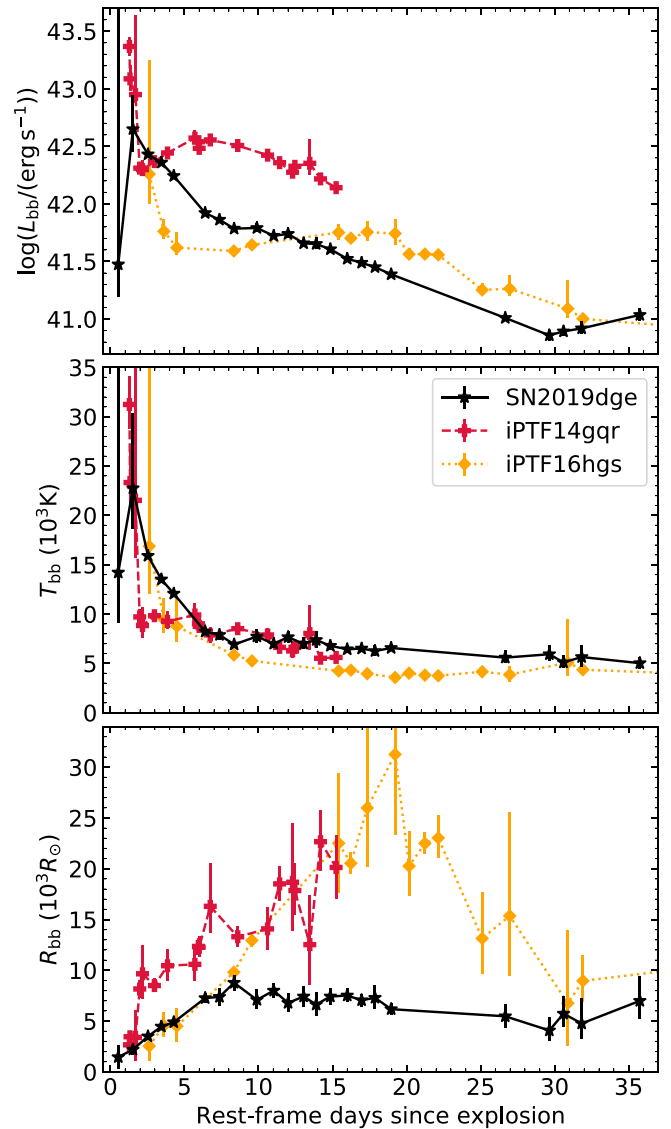


Figure 4. Evolution of blackbody properties (luminosity, temperature, radius) over time of SN2019dge compared with iPTF14gqr and iPTF16hgs. We use the same method as applied in SN2019dge to derive L_{bb} , T_{bb} , and R_{bb} for iPTF14gqr and iPTF16hgs.

The bottom panel of Figure 3 shows that t_{decay} of SN2019dge is longer than that for the most rapid-fading SNe Ibc, such as SN2005ek, SN2018kzr, and SN2019bkc. Its decay timescale is more similar to SN2002bj, SN2010X, the population of Ca-rich transients (PTF09dav, PTF10iuv, iPTF16hgs), and likely iPTF14gqr. It has been suggested that the latter group of events has a radioactivity-powered main peak with a low mass of nickel ($M_{\text{Ni}} \lesssim 0.1 M_{\odot}$).

3.1.2. Bolometric Evolution

We construct the bolometric light curve at epochs where at least detections in two filters are available by fitting the spectral energy distribution (SED) with a blackbody function (see details of model fitting in Appendix B.1). We plot the physical evolution of SN2019dge with comparisons to iPTF14gqr and iPTF16hgs in Figure 4, in which we have adopted the explosion epoch of iPTF14gqr, iPTF16hgs, and SN2019dge estimated by De et al. (2018c, 2018b), and Section 4.1 of this paper, respectively. The bolometric luminosity of SN2019dge

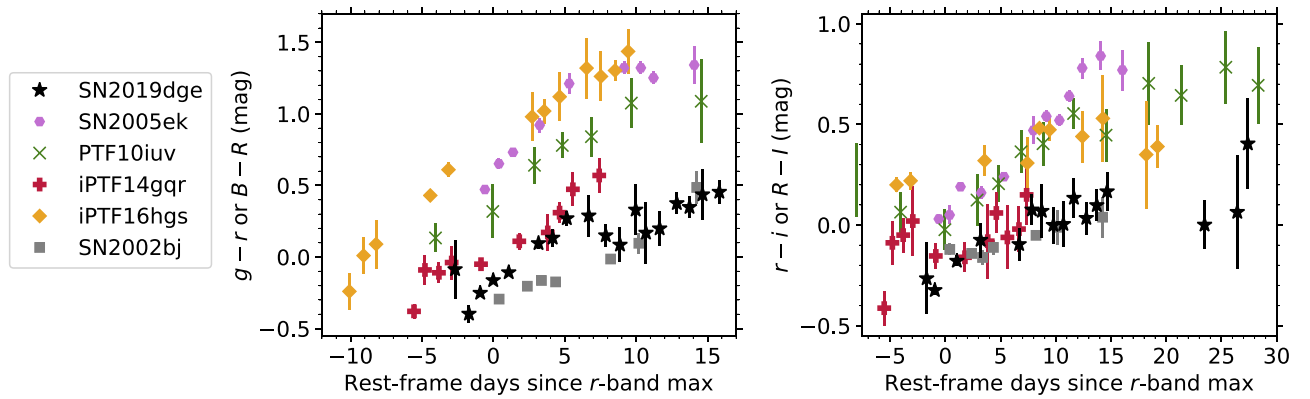


Figure 5. Comparison of the color evolution of SN2019dge with a subset of fast SNe shown in Figure 3. All colors have been corrected for Galactic extinction. Because of the absence of photometry in identical filters, we compare colors in corresponding filter pairs of B/g , R/r , and I/i . Because all SNe shown here are at relatively low redshifts ($z \lesssim 0.063$), the observed colors probe similar rest-frame bands.

reaches $\sim 5 \times 10^{42} \text{ erg s}^{-1}$ at ~ 1.5 days after the explosion epoch. The subsequent decline displays an initial fast drop of $0.36 \text{ mag days}^{-1}$ at age 2–9 days, and transitions to a slower drop of $0.11 \text{ mag days}^{-1}$ at age 10–30 days.

The bolometric temperature of SN2019dge reaches as high as $\sim 2.3 \times 10^4 \text{ K}$ at age 1.5 days and rapidly falls afterwards. The maximum T_{bb} is much hotter than that observed in normal SNe Ibc (6000–10,000 K, Taddia et al. 2018). Its early light-curve evolution is slower than iPTF14gqr, but similar to iPTF16hgs and several other stripped envelope SNe displaying double-peaked light curves (e.g., see Figure 2 of Fremling et al. 2019). Their first peaks have been modeled by cooling emission from an extended envelope around the progenitor after the core-collapse SN (CCSN) shock breaks out (Modjaz et al. 2019). After ~ 8 days past explosion, T_{bb} flattens to $6000 \pm 1000 \text{ K}$, similar to the behavior of normal SNe Ibc at a much later phase (~ 30 days after explosion, Taddia et al. 2018).

Assuming that the photospheric radius can be approximated by R_{bb} and linearly expands at early phase, we fit a linear function to the first few R_{bb} versus time measurements of SN2019dge, which gives $\approx 8000 \text{ km s}^{-1}$. The radius then remains flat at $\sim 6.7 \times 10^3 R_{\odot}$ during age 8–30 days, and even appears to slowly recede. The reason for this is that the temperature drops to a recombination temperature for helium and the opacity becomes small. As a result, the outer layers of the ejecta become more transparent, and deeper regions of the ejecta are being probed (Piro & Morozova 2014).

3.1.3. Color Evolution

We compare the color curves of other fast transients to that of SN2019dge in Figure 5, in corresponding pairs of $g-r$ (or $B-R$) and $r-i$ (or $R-I$). For the double-peaked events iPTF14gqr and iPTF16hgs, “maximum” time corresponds to epoch of maximum light in the second peak.

The early-time blue color of SN2019dge arises from the high-temperature peak. Among other events, SN2002bj, iPTF14gqr, and iPTF16hgs exhibit early colors as blue as SN2019dge. Subsequently, SN2019dge displays a color starting out blue and turning redder with time, consistent with a cooling process.

One unusual feature of SN2019dge is that at ~ 6 –9 days after maximum light, the $g-r$ color becomes bluer by $\approx 0.2 \text{ mag}$, while after that the color continues to redden. We notice that

iPTF14gqr exhibits a similar trend—around 4 days before the second peak, its $g-r$ color stays flat before getting redder afterwards, while around 2 days before the second peak, its $r-i$ color also turns bluer by $\approx 0.2 \text{ mag}$.

3.2. Spectroscopic Properties

3.2.1. Early Spectral Evolution

The very early spectra at -1.1 , -0.1 , and $+0.4$ days show a blue continuum and strong galaxy emission lines from the underlying H II region (see Figure 6). In addition, these spectra also show prominent He I $\lambda 5876$ and high-ionization He II $\lambda 4686$ narrow emission lines. We computed the equivalent width (EW) of He II emission using the spectral line and continuum wavelength ranges given by Khazov et al. (2016). The EW is found to be $-7.56 \pm 1.07 \text{ \AA}$, $-2.66 \pm 1.30 \text{ \AA}$, and $-3.77 \pm 0.16 \text{ \AA}$ in the -1.1 days, -0.1 days, and $+0.4$ days spectra.

In Table 2, we show the measured FWHM velocities of some emission lines by fitting a Gaussian to the line profile. Because the [S II] $\lambda\lambda 6716, 6731$ doublet is definitely from the host galaxy, their line widths serve as a practical measurement of instrumental line-broadening. As shown in column 2, FWHM velocities of the He II and He I emission lines are $\sim 550 \text{ km s}^{-1}$ and $\sim 580 \text{ km s}^{-1}$, much broader than the resolution of $\approx 270 \text{ km s}^{-1}$, whereas H α is not well resolved. Thus, we infer that the hydrogen emission is from the host galaxy, while the helium lines are from photoionized material exterior to the SN.

3.2.2. Photospheric Phase Spectral Evolution

Broad transient features are present in the $+12.0$ and $+14.3$ days spectra (Figure 7). These spectra are taken at the photospheric phase where emission comes from a photosphere receding (in mass coordinates) back through freely expanding SN ejecta. The HST spectrum contains little host-galaxy contamination due to its high angular resolution. Prominent galaxy emission lines in the DBSP spectrum are identified and plotted in light red to emphasize transient features. The existence of the P-Cygni He I $\lambda 5876$ profile and nonexistence of hydrogen nominally classify SN2019dge as a Type Ib SN. We measure the velocity of the He I $\lambda 5876$ line by fitting a parabola to the absorption minimum. The resulting fits give velocities of $\approx 6000 \text{ km s}^{-1}$ and 5900 km s^{-1} for the

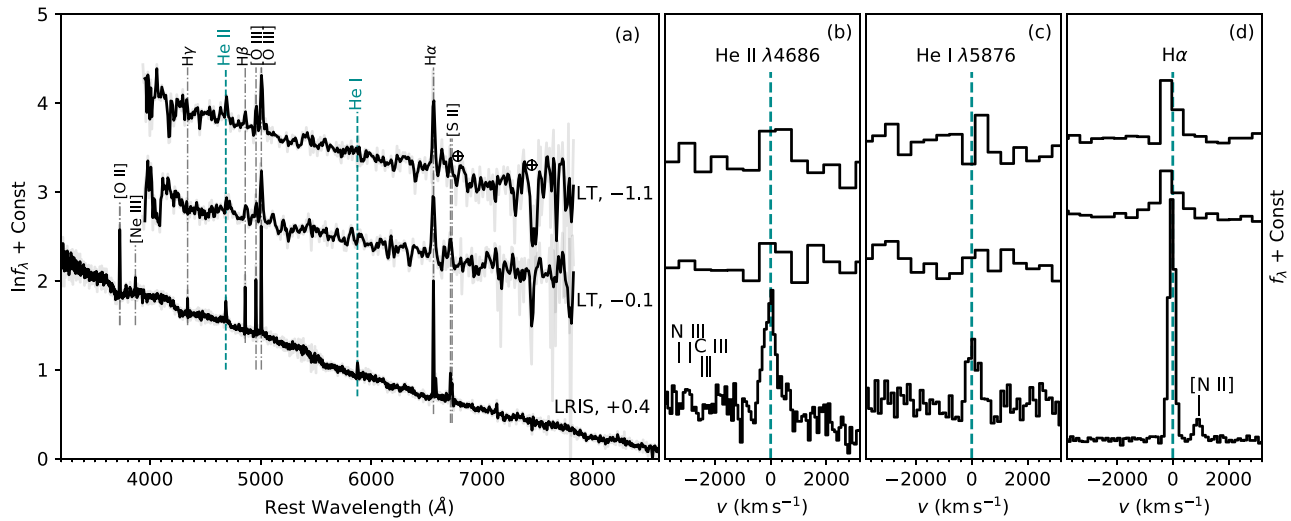


Figure 6. Early-time spectra of SN2019dge. In panel (a), the original spectra are shown in translucent colors, with the overlying black lines showing the same spectra convolved with an FWHM = 800 km s⁻¹ (for LT) or FWHM = 200 km s⁻¹ (for LRIS) Gaussian kernel. Prominent galaxy lines are marked by the dashed-dotted lines. In panels (b), (c), and (d), we show the observed spectra (not convolved) in velocity space around the He II 44686, He I 5876, and H α emission lines.

Table 2

Rest-frame FWHM (km s⁻¹) of Narrow Emission Lines in the +0.4 days, +85.3 days, and +314.4 days LRIS Spectra

Transition	+0.4 days	+85.3 days	+314.4 days
He II λ 4686	552 \pm 36
He I λ 5876	582 \pm 86	272 \pm 19	298 \pm 24
He I λ 6678	...	282 \pm 28	339 \pm 59
He I λ 7065	...	230 \pm 37	218 \pm 26
H α	291 \pm 49	263 \pm 13	280 \pm 14
[S II] λ 6716	285 \pm 52	254 \pm 14	274 \pm 18
[S II] λ 6731	263 \pm 78	251 \pm 14	264 \pm 15
[O I] λ 6300	...	263 \pm 28	231 \pm 24

+12.0 days and +14.3 days spectra, respectively. This is lower than velocities of normal SNe Ib measured from the He I λ 5876 absorption minimum ($\sim 10^4$ km s⁻¹, Liu et al. 2016), but higher than that in Type Ibn SNe (~ 3000 km s⁻¹, Hosseinzadeh et al. 2017).

In Figure 8, we compare the photospheric phase optical spectra of SN2019dge with other helium-rich events. Note that the DBSP spectrum has host emission lines masked. SN2019dge is different from normal helium-rich stripped envelope SNe Ib/Ib or SNe Ibn in the sense that its P-Cygni absorption minimum in the He I λ 5876 line is weaker. The feature at ~ 5000 Å is often attributed to He I λ 5016 and Fe II triplet $\lambda\lambda$ 4924, 5018, and 5169 (Liu et al. 2016). The shape of this feature in SN2019dge is similar to those in normal SNe Ib/Ib at much later phases (~ 20 days post maximum), indicating that the spectral evolution of SN2019dge is faster. The complex absorption profile at ~ 4500 Å has been identified as a blend of Fe II, Mg II λ 4481, and He I λ 4472 (Hamuy et al. 2002). In the DBSP spectrum, we detected O I λ 7774 and broad Ca II at ~ 8500 Å (due to the $\lambda\lambda$ 8498, 8542, and 8662 triplet) with clear P-Cygni profiles. Both are major features of stripped envelope SNe (Gal-Yam 2017).

In Figure 9, we compare the HST NUV spectrum with spectra of other types of SNe. The UV part of SN2019dge is much weaker than a blackbody extrapolation of the optical spectra would predict. This has also been seen in normal thermonuclear and CCSNe, and interpreted as strong metal-line

blanketing caused by iron-peak elements, particularly Fe II and Co II (Gal-Yam et al. 2008). SN2019dge bears a close resemblance to SN1993J between 2000 Å and 4000 Å. In Figure 9, we also marked the rest wavelength of Mg I λ 2852 and Mg II $\lambda\lambda$ 2796, 2803. The emission features at ~ 2760 Å in SN2019dge and Gaia16apd are similar to the bump at ~ 2730 Å in SN1993J, which was found to be a NLTE Mg II emission line (Jeffery et al. 1994). This resonance line is blueshifted from its rest wavelength, and is suggested to come from a circumstellar region that is distinctly separated from the SN photosphere in velocity and excitation conditions (Panagia et al. 1980; Fransson et al. 1984).

3.2.3. Late-time Spectral Evolution

Figure 10 shows late-time spectra of SN2019dge obtained at +85.3, +143.1, +171.1, and +314.4 days. The general shape of the spectra is determined by the host galaxy, while possible SN features are marked by the dashed lines. The right panels (b), (c), and (d) highlight emission lines at wavelengths of He I, [O I], and [Ca II]. In panel (c) of Figure 10, the [O I] $\lambda\lambda$ 6300, 6363 feature consists of two narrow emission peaks. These doublet transitions share the same upper level ($^3P_{1,2}^{-1}D_2$). The observed intensity ratio $R \equiv F(6300/6364) \sim 3.1$ agrees with the nebular condition, as one would expect in the optically thin regime (Leibundgut et al. 1991; Li & McCray 1992). In panel (d), we mark the position of the [Ca II] doublet in dashed lines, but only the λ 7324 line is clearly detected. It presents a double-peaked profile with a peak separation of ~ 400 km s⁻¹.

From panel (a) of Figure 10, it is also clear that in the +85.3 days spectrum, the He I and [Ca II] lines have broader emission components with Lorentzian profiles at the bases of the narrow emission lines. These Lorentz-shaped components are not visible in the +314.4 days spectrum. Therefore, to further investigate the broader features, we subtract the +314.4 days' spectrum from the +85.3 days spectrum. The resulting subtraction (Figure 11) reveals intermediate-width (FWHM ~ 2000 km s⁻¹) components of He I, [Ca II], and the Ca II IR triplet. It shares a close resemblance to some Type Ibn SNe, such as SN2011hw (Pastorello et al. 2015) and SN2015G (Shivvers et al. 2017). These intermediate-width

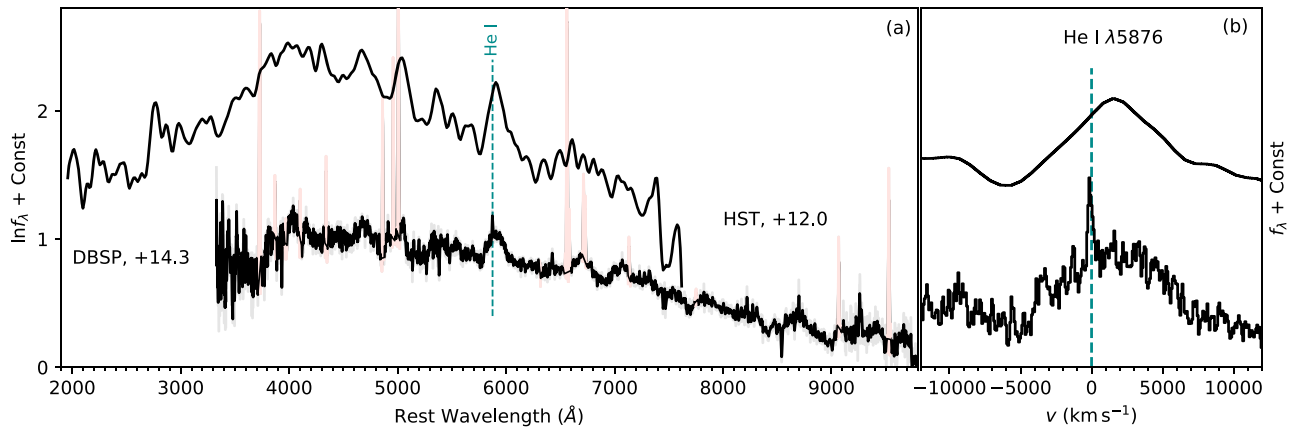


Figure 7. Photospheric phase spectra of SN2019dge. In panel (a), the original DBSP spectrum is shown in translucent colors, with the overlying black lines showing the same spectrum convolved with an $\text{FWHM} = 200 \text{ km s}^{-1}$ Gaussian kernel. We mask prominent galaxy lines in the DBSP spectrum in light red. In panel (b), we show the observed spectra (not convolved with any kernels) in velocity space around He I $\lambda 5876$.

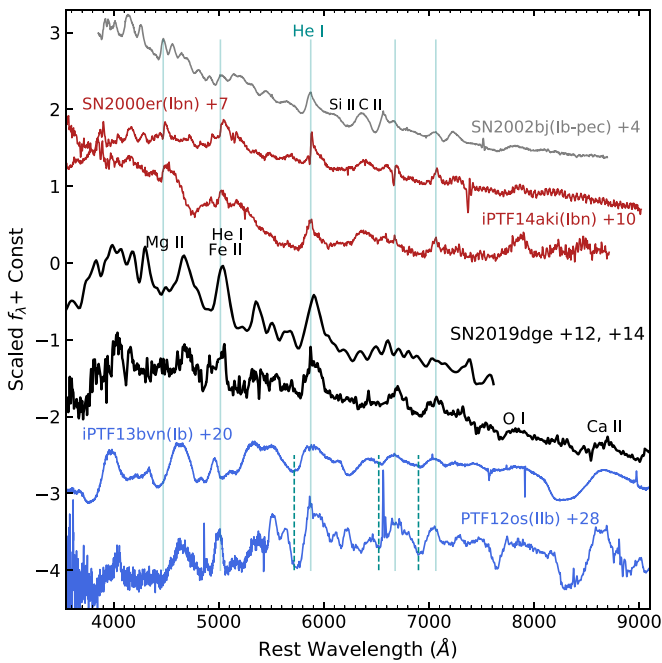


Figure 8. Photospheric phase spectra of SN2019dge compared with other SNe, including SN2000er (Pastorello et al. 2008), SN2002bj (Poznanski et al. 2010), iPTF14aki (Hosseinzadeh et al. 2017), PTF12os, and iPTF13bvn (Fremling et al. 2016). He I transitions at rest wavelength are marked by the vertical cyan lines (though note that not all of these lines are visible in all spectra shown here).

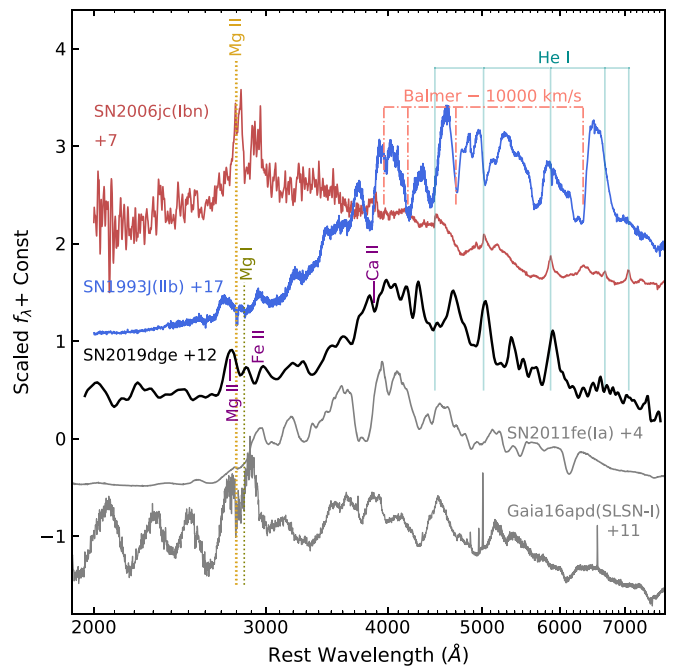


Figure 9. HST spectrum of SN2019dge compared with other SNe, including SN2006jc (Bufano et al. 2009), SN1993J (Jeffery et al. 1994), SN2011fe (Mazzali et al. 2014), and Gaia16apd (Yan et al. 2017). The slightly blueshifted Mg II $\lambda 2800$ emission feature is observed in SN2006jc, SN1993J, SN2019dge, and Gaia16apd.

features are too narrow to be explained by emission from SN ejecta. Instead, they are probably emitted by a cold, dense circumstellar medium (CSM) shell formed by radiative cooling from the post-shock material, as has been proposed to be the case in interacting Type II_n/Ib_n SNe (Chugai & Danziger 1994; Smith 2017).

Table 2 (column 3 and 4) gives the measured FWHM velocities of narrow emissions shown in panels (b), (c), and (d) of Figure 10. It can be seen that the measured FWHM of other emission lines are similar to the [S II] line width. Therefore, we conclude that the observed narrow emissions are not resolved.

Because of the low resolution of our LRIS spectra, we cannot directly rule out the possibility that the narrow lines are emanating from the host galaxy. However, there is evidence

indicating that they are not merely a background contamination of an underlying H II region:

1. In the +85.3 days spectrum, the He I and [Ca II] narrow emissions are on top of intermediate-width Lorentzian components characteristic of electron scattering (Huang & Chevalier 2018), which fades away in the +314.4 days' spectrum. However, the hydrogen Balmer lines do not have a broader base in any of our spectra.
2. The flux intensities of He I, [O I], and [Ca II] lines decrease by a factor of approximately 2 from +85.3 days to +314.4 days, consistent with the temporal evolution from an emission mechanism connected to the aging supernova. As a comparison, the line strengths of the strongest emissions in normal ionized nebulae ($\text{H}\alpha$, [O III], [O II], [S II], etc.) do not follow this behavior.

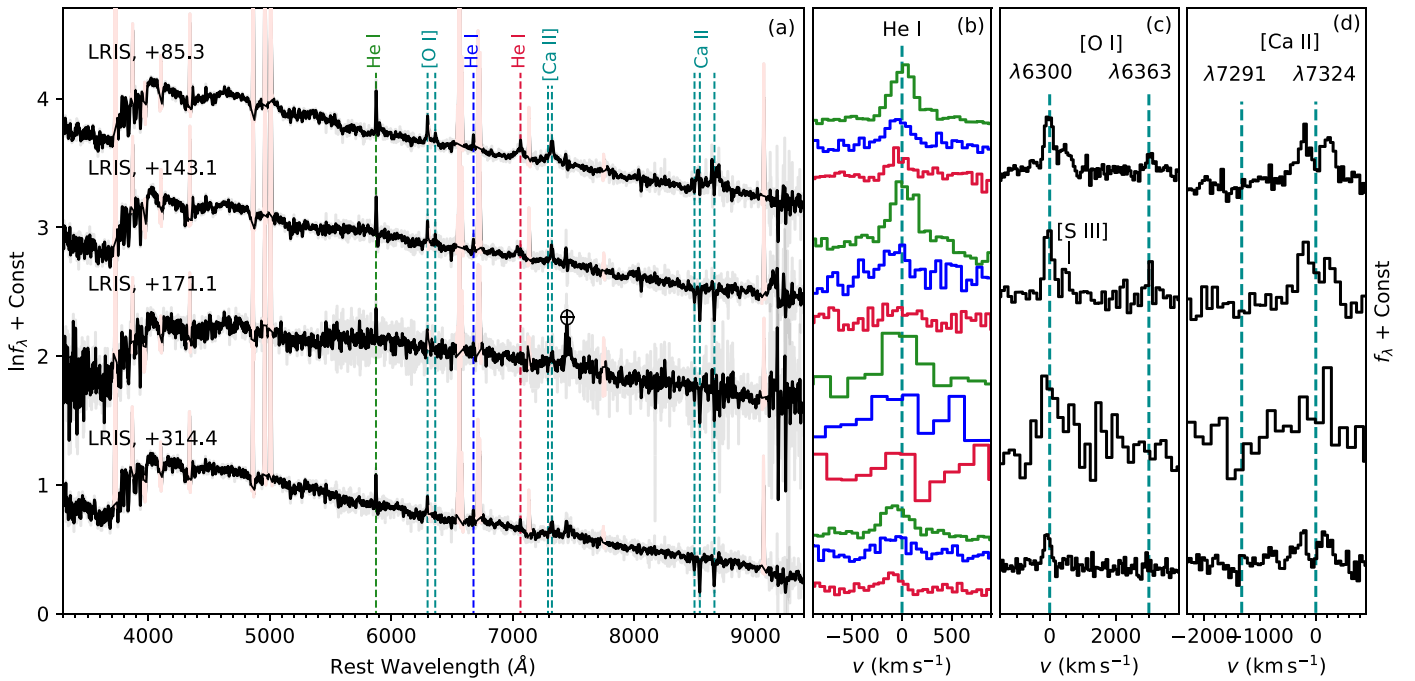


Figure 10. Late-time spectra of SN2019dge. In panel (a), the original spectra are shown in translucent colors, with the overlying black lines showing the same spectra convolved with $\text{FWHM} = 200 \text{ km s}^{-1}$ Gaussian kernels. We mask prominent galaxy lines in light red. Possible SN features are marked by the dashed lines. In panels (b), (c), and (d), the spectra at phase +85.3 days, +143.1 days, +171.1 days, and +314.4 days are binned by 1, 2, 3, and 1 pixel(s), respectively (1.16 Å per pixel). The binning factors are chosen based on the different signal-to-noise ratio (S/N) in these spectra (see exposure times in Table 1). Note that in panel (b), we plot evolution of He I $\lambda 5876$, $\lambda 6678$, and $\lambda 7065$ emissions in green, blue, and crimson, respectively.

3. Although the He I and [O I] lines labeled in panel (a) of Figure 10 have been observed in H II regions (Peimbert et al. 2000, 2017), the doublet [Ca II] $\lambda\lambda 7291, 7324$ has not been detected in gaseous nebulae (Kingdon et al. 1995).

Taken together, we suggest that the narrow components ($\lesssim 270 \text{ km s}^{-1}$) of He I, [Ca II], [O I], and Ca II are also associated with the transient. Their widths might be consistent with the typical velocities of pre-shock CSM. The detection of these lines at >300 days after the SN explosion suggests that the circumstellar shell extends to $\gtrsim 2 \times 10^{16} \text{ cm}$ ($\sim 1000 \text{ au}$) from the progenitor.²¹

4. Modeling

4.1. Shock Cooling Powered Fast Rise

Supernovae light curves are mainly powered by shock energy or radiative diffusion from a heating source. We first examine if the peak of SN2019dge is likely to be powered by the radioactive decay of $^{56}\text{Ni} \rightarrow ^{56}\text{Co} \rightarrow ^{56}\text{Fe}$. With a peak luminosity of $L_{\text{peak}} \approx 5 \times 10^{42} \text{ erg s}^{-1}$ and a rise time of $t_{\text{peak}} \approx 2\text{--}4$ days, SN2019dge falls into the unshaded region of Kasen (2017, their Figure 1), where an unphysical condition of $M_{\text{Ni}} > M_{\text{ej}}$ is required. Therefore, we rule out radioactivity as the power source for the fast rise of the light curve.

There have been clues for the early emission mechanism of SN2019dge,:

1. The fast t_{rise} (Figure 3), initial high temperature (middle panel of Figure 4), blue color (Figure 5), and relatively fast color evolution of SN2019dge are reminiscent of

shock cooling emission (SCE, Nakar & Piro 2014; Piro 2015; Piro et al. 2020).

2. The color jump in $g - r$ is observed 6–9 days after maximum (left panel of Figure 5). It is roughly at the change in bolometric luminosity decline rate transitions from $0.36 \text{ mag days}^{-1}$ to $0.11 \text{ mag days}^{-1}$ (upper panel of Figure 4). This supports the idea that the dominant power mechanisms before and after this transition are different.

Therefore, we model the early light curve as cooling emission from shock-heated extended material, which is located at the outer layers of the progenitor or outside of the progenitor. We use models presented by (Piro et al. 2020, hereafter P20) to constrain the mass, radius, and energy of the extended material (M_{ext} , R_{ext} , and E_{ext} , respectively). Compared with the SCE model introduced in Piro (2015), P20 does a better job of resolving the velocity gradient in the ejecta, and the velocity is higher near the surface of the material. Details of the model fitting to multiband observations are illustrated in Appendix B.2.

In Figure 12, the bolometric light curve measured in Section 3.1 is shown in black. We also show late-time r -band νL_{ν} measurements in gray empty circles as a proxy of bolometric light-curve evolution. The dashed green line shows the best-fit model of $M_{\text{ext}} = 9.71^{+0.28}_{-0.27} \times 10^{-2} M_{\odot}$, $R_{\text{ext}} = 1.19^{+0.06}_{-0.05} \times 10^{13} \text{ cm}$ (i.e., $171.2^{+8.3}_{-7.7} R_{\odot}$), $E_{\text{ext}} = (5.30^{+0.25}_{-0.24}) \times 10^{49} \text{ erg}$, and explosion epoch at phase $t_{\text{exp}} = -2.91 \pm 0.02$ days.

Given the simple assumptions of the model, we expect the constraints on M_{ext} and R_{ext} to be only approximately accurate. We thus conclude that the early shock cooling emission was produced by an extended envelope with a mass of $\sim 0.1 M_{\odot}$ located at a radius of $\sim 1.2 \times 10^{13} \text{ cm}$ ($170 R_{\odot}$).

²¹ Adopting a conservative shock velocity estimation of $v_s \approx 10^4 \text{ km s}^{-1}$, the forward shock travels $2.6 \times 10^{16} \text{ cm}$ after 300 days.

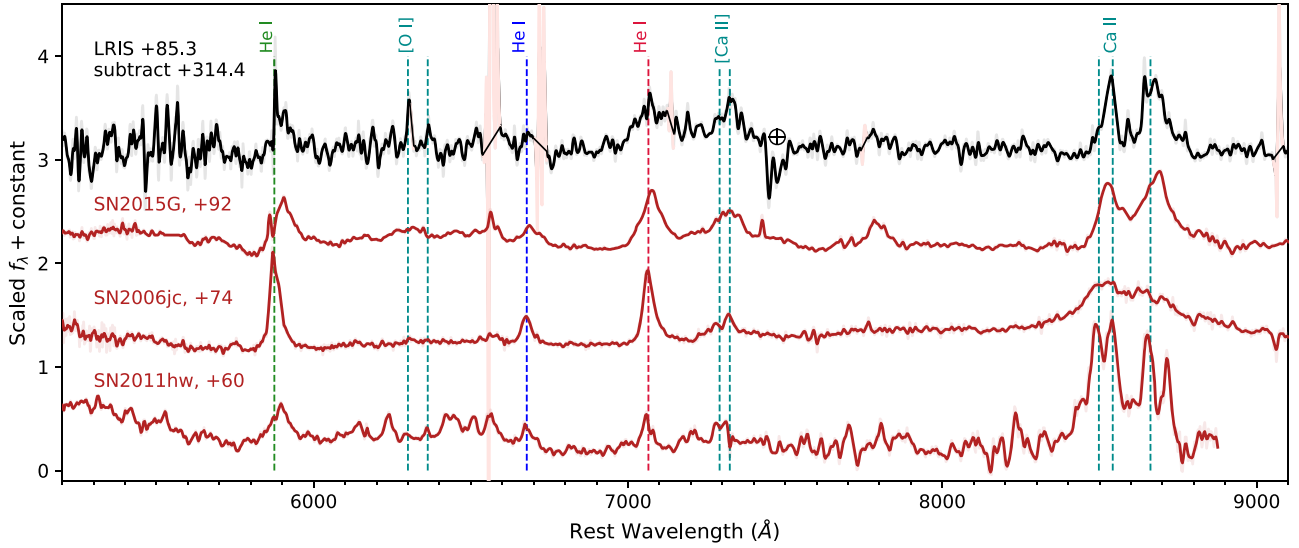


Figure 11. Subtracted late-time spectrum of SN2019dge compared with Type Ib SNs SN2006jc (Shivvers et al. 2019), SN2011hw (Pastorello et al. 2015), and SN2015G (Shivvers et al. 2017).

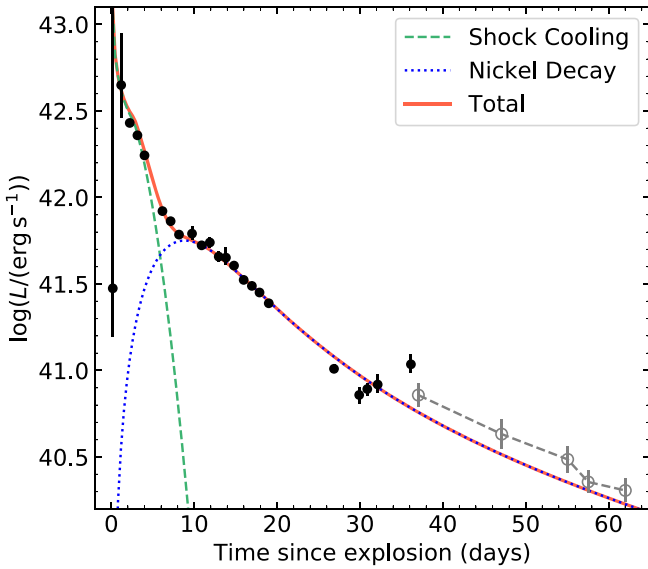


Figure 12. Bolometric light curve for SN2019dge. Late-time quasi-bolometric light curve estimated by computing νL_ν in r band is shown as empty gray circles. The dashed green and dotted blue lines show the best fits of shock cooling and nickel decay models. The solid red line shows the combination of the two components.

4.2. Mass-loss Estimate from He II

Early-time low-velocity He II $\lambda 4686$ emission (Section 3.2.1) has been detected in nearly 20 hydrogen-rich CCSNe and one hydrogen-poor SN, iPTF14gqr. This feature often fades away a few hours to a few days after the explosion (Yaron et al. 2017). The high ionization potential of this line requires high temperature or an ionizing flux, which might come from either shock breakout or CSM interaction (Gal-Yam et al. 2014; Smith et al. 2015). Because of the rapid decrease in T_{bb} at the three epochs of our early-time spectra and the similarity between SN2019dge and iPTF14gqr, we favor shock cooling emission as the origin of recombination helium lines. Therefore, we can use the luminosity of the He II $\lambda 4686$ line to make an order-of-magnitude estimate on properties of the

emission material, following the procedure given by Ofek et al. (2013b) and De et al. (2018c).

Assuming that the immediate CSM around the progenitor has a spherical wind-density profile of the form, $\rho = K r^{-2}$, where r is distance from the progenitor, $K \equiv \dot{M}/(4\pi v_w)$ is the wind-density parameter, v_w is the wind velocity, and \dot{M} is the mass-loss rate. The integrated mass of the emitting material from r to r_1 is

$$M_{\text{He}} = \int_r^{r_1} 4\pi r^2 \rho(r) dr = 4\pi K \beta r \quad (1)$$

where $\beta \equiv (r_1 - r)/r$ is assumed to be of order unity.

We can relate the mass of the He II region to the He II $\lambda 4686$ line luminosity using

$$L_{\lambda 4686} \approx \frac{A n_e M_{\text{He}}}{m_{\text{He}}}. \quad (2)$$

Here

$$A = \frac{4\pi j_{\lambda 4686}}{n_e n_{\text{He}^{2+}}}, \quad (3)$$

where $j_{\lambda 4686}$ (in $\text{erg cm}^{-3} \text{s}^{-1} \text{sr}^{-1}$) is the emission coefficient for the $\lambda 4686$ transition. m_{He} is mass of a helium nucleus, $n_{\text{He}^{2+}}$ is the number density of doubly ionized helium, and n_e is the number density of electrons.

Assuming a temperature of 10^4 K, electron density of 10^{10} cm^{-3} , and Case B recombination, we get $A = 1.32 \times 10^{-24} \text{ erg cm}^3 \text{ s}^{-1}$ (Storey & Hummer 1995). Using $n_e = 2n_{\text{He}^{2+}}$ and the density profile, Equation (2) can be written as

$$L_{\lambda 4686} \approx \frac{8\pi A \beta K^2}{m_{\text{He}}^2 r}. \quad (4)$$

The location of the emitting region can be constrained by requiring that the Thompson optical depth (τ) in the region must be small for the lines to escape. We require

$$\tau = n_e \sigma_T \int_r^{r_1} dr = \frac{2\sigma_T K \beta}{m_{\text{He}} r} \lesssim 1 \quad (5)$$

Thus

$$r^2 \gtrsim \left(\frac{2\sigma_T\beta}{m_{\text{He}}} \right)^2 \frac{L_{\lambda 4686} m_{\text{He}}^2 r}{8\pi A\beta} \quad (6a)$$

$$r \gtrsim L_{\lambda 4686} \frac{\sigma_T^2 \beta}{2\pi A} \quad (6b)$$

The +0.4 days emission line flux is measured to be $F = (8.99 \pm 0.71) \times 10^{-16} \text{ erg cm}^{-2} \text{ s}^{-1}$, corresponding to $L_{\lambda 4686} = 9.0 \times 10^{38} \text{ erg s}^{-1}$. Hence, we get $r \gtrsim 4.8 \times 10^{13} \beta \text{ cm}$, $K \gtrsim 1.2 \times 10^{14} \text{ g cm}^{-1}$, and $M_{\text{He}} \gtrsim 3.7 \times 10^{-5} \beta^2 M_{\odot}$. Adopting a wind velocity of $v_w \approx 550 \text{ km s}^{-1}$ as measured from the He II FWHM, the mass-loss rate can be constrained to be $\dot{M} \gtrsim 1.1 \times 10^{-4} M_{\odot} \text{ yr}^{-1}$. Note that these estimates can be affected if the CSM cannot be well characterized by a spherically symmetric $\rho(r) \propto r^{-2}$ density profile, or if the emitting region was confined to a thin shell ($\beta \ll 1$). Our radio upper limits are not deep enough to place stringent constraints on the mass-loss parameters (see details in Appendix B.5).

4.3. Radioactivity-powered Main Peak

After subtracting the SCE from the bolometric light curve, the remaining light curve has a peak luminosity of $L_{\text{peak}} \approx 6 \times 10^{41} \text{ erg s}^{-1}$ and a rise time of $t_{\text{peak}} \approx 9 \text{ d}$. In the shaded region of Kasen (2017, Figure 1), this falls between the $M_{\text{Ni}} = 0.1 M_{\text{ej}}$ and $M_{\text{Ni}} = 0.01 M_{\text{ej}}$ lines, indicating that the remaining component can be powered by ^{56}Ni decay. Apart from this, the moderate t_{decay} of SN2019dge (bottom panel in Figure 3) is similar to that found in a few Ca-rich transients, and consistent with coming from radioactivity. Here we use two methods to estimate M_{ej} and M_{Ni} .

First of all, we use analytical models (Arnett 1982; Valenti et al. 2008; Wheeler et al. 2015) to constrain the nickel mass (M_{Ni}), a characteristic photon diffusion timescale (τ_m), and a characteristic γ -ray escape timescale (t_0). Details of the model fitting are given in Appendix B.3. The dotted blue line in Figure 12 shows the best-fit model of $M_{\text{Ni}} = 1.57_{-0.03}^{+0.04} \times 10^{-2} M_{\odot}$, $\tau_m = 6.53_{-0.17}^{+0.18} \text{ days}$, and $t_0 = 23.86_{-0.76}^{+0.78} \text{ days}$. Thus, using Equation (B6), the ejecta mass can be estimated to be

$$M_{\text{ej}} = 0.38 \pm 0.02 \left(\frac{v_{\text{ej}}}{8000 \text{ km s}^{-1}} \right) \left(\frac{0.07 \text{ cm}^2 \text{ g}^{-1}}{\kappa_{\text{opt}}} \right) M_{\odot} \quad (7)$$

Here we adopt the mean opacity of SNe Ibc found by Taddia et al. (2018). In Section 3.2.2, the photospheric velocity of $\approx 6000 \text{ km s}^{-1}$ is measured at phase $\Delta t \sim 12 \text{ days}$ (i.e., $\sim 15 \text{ days}$ post explosion). At that time, Figure 4 shows that R_{bb} stays roughly flat, indicating that a certain amount of ejecta in the outer layers should have a velocity greater than that measured from the He I absorption minimum. Therefore, we adopt the $\approx 8000 \text{ km s}^{-1}$ measured from early R_{bb} evolution (see Section 3.1.2) to be a more appropriate estimate for v_{ej} . The kinetic energy is then calculated to be

$$E_{\text{kin}} = \frac{3}{10} M_{\text{ej}} v_{\text{ej}}^2 = (1.44 \pm 0.08) \times 10^{50} \text{ erg} \quad (8)$$

Khatami & Kasen (2019, hereafter KK19) presented improved analytic relations (compared with the original Arnett 1982 model) between t_{peak} and L_{peak} . When $t < 10 \text{ days}$, $\varepsilon_{\text{Ni}}(t) \gg \varepsilon_{\text{Co}}(t)$ (see Equations (B2) and (B3)), and hence we

have an exponential heating function

$$L_{\text{heat}}(t) = L_0 e^{-t/\tau_{\text{Ni}}} \quad (9)$$

where $L_0 = M_{\text{Ni}} \times \varepsilon_{\text{Ni}}$. In this case, KK19 (Equation (21)) shows that the relation between peak time and luminosity is

$$L_{\text{peak}} = \frac{2L_0 \tau_{\text{Ni}}^2}{\beta^2 t_{\text{peak}}^2} [1 - (1 + \beta t_{\text{peak}}/\tau_{\text{Ni}}) e^{-\beta t_{\text{peak}}/\tau_{\text{Ni}}}] \quad (10)$$

where $\beta \sim 4/3$ gives a reasonable match to numerical simulations. With $L_{\text{peak}} \approx 6 \times 10^{41} \text{ erg s}^{-1}$ and $t_{\text{peak}} \approx 9 \text{ days}$, we get an estimate of $M_{\text{Ni}} \sim 0.017 M_{\odot}$.

M_{ej} can be estimated using Equation (23) of KK19:

$$\frac{t_{\text{peak}}}{t_d} = 0.11 \ln \left(1 + \frac{9\tau_{\text{Ni}}}{t_d} \right) + 0.36, \quad (11)$$

where t_d is the characteristic timescale without any numerical factors

$$t_d = \left(\frac{\kappa_{\text{opt}} M_{\text{ej}}}{v_{\text{ej}} c} \right)^{1/2}. \quad (12)$$

We derive $t_d \approx 15.4 \text{ days}$, which implies

$$M_{\text{ej}} \approx 0.33 \left(\frac{v_{\text{ej}}}{8000 \text{ km s}^{-1}} \right) \left(\frac{0.07 \text{ cm}^2 \text{ g}^{-1}}{\kappa_{\text{opt}}} \right) M_{\odot} \quad (13)$$

The kinetic energy of the ejecta is then $E_{\text{kin}} \approx 1.3 \times 10^{50} \text{ erg}$.

In conclusion, the estimates derived from simplified model fitting and new analytic relations from KK19 are roughly the same. The ejecta mass ($M_{\text{ej}} \sim 0.3 M_{\odot}$), the nickel mass ($M_{\text{Ni}} \sim 0.017 M_{\odot}$), and the total kinetic energy ($E_{\text{kin}} \sim 1.3 \times 10^{50} \text{ erg}$) of SN2019dge are very small.

5. Interpretation

5.1. A Core-collapse Supernova

At early times, the cooling emission from shock-heated surrounding material of $M_{\text{ext}} \sim 0.1 M_{\odot}$ and $R_{\text{ext}} \sim 1.2 \times 10^{13} \text{ cm}$ ($170 R_{\odot}$) corroborates that the progenitor of SN2019dge is a star with an extended envelope. Indeed, stellar evolution models predict envelope radii of 10–200 R_{\odot} for helium stars with zero-age helium core masses within 2.5–3.2 M_{\odot} that have stripped all of the hydrogen-rich envelope (Woosley 2019; Laplace et al. 2020). Therefore, the early-time shock cooling light curve serves as strong evidence that SN2019dge is the explosion of a star with inflated radius (not a compact object).

The ^{56}Ni mass of $\sim 0.017 M_{\odot}$ inferred from the radioactivity-powered decay is much greater than that produced in electron-capture SNe ($\sim 10^{-3} M_{\odot}$, Moriya et al. 2014), whereas the ejecta velocity of $\approx 8000 \text{ km s}^{-1}$ is larger than that expected in fallback SNe ($\sim 3000 \text{ km s}^{-1}$; Moriya et al. 2010). Therefore, we conclude that SN2019dge is associated with the class of Fe CCSNe.

5.2. An Ultra-stripped Progenitor

As noted in the introduction, the majority of SNe Ibc, with M_{ej} in the range of 1–5 M_{\odot} , are believed to come from binary evolution. The small amount of ejecta mass seen in SN2019dge ($M_{\text{ej}} \sim 0.3 M_{\odot}$) requires extreme stripping prior to the

explosion in a binary system, which suggests an ultra-stripped progenitor (Tauris et al. 2013).

Compared with iPTF14gqr, in which the second peak of the light curve suggests $M_{\text{ej}} \sim 0.2 M_{\odot}$, SN2019dge has a higher ejecta mass. In particular, the helium-rich photospheric spectra indicate that SN2019dge has a greater amount of helium in the ejecta. He I emission lines are nonthermally excited by collisions with fast electrons, which result from Compton processes with γ -rays from ^{56}Ni decay (Dessart et al. 2012; Hachinger et al. 2012). On the other hand, the weak absorption strength in the He I P-Cygni profile (Figures 7 and 8) suggests that the helium envelope mass of SN2019dge is substantially lower than that in a canonical Type Ib SN (Fremling et al. 2018). While the stripping in SN2019dge is less extreme than for iPTF14gqr, the striking similarities between these two events indicate that they probably originate from similar channels.

The He II $\lambda 4686$ flash-ionized emission comes from optically thin material located at $\sim 5 \times 10^{13}$ cm ($700 R_{\odot}$). This is even larger than the expected orbital separation required for extreme stripping. Therefore, material at such a large radius might be ejected prior to the explosion, with a mass-loss timescale $t \sim 5 \times 10^{13}$ cm / (500 km s^{-1}) ~ 10 d. The inferred mass-loss rate of $\dot{M} \gtrsim 10^{-4} M_{\odot} \text{ yr}^{-1}$ is much higher than that observed in Galactic Wolf-Rayet stars (Smith 2014). Additionally, the photospheric and late-time spectra of SN2019dge signify interaction with a helium-rich extended dense shell, which may also consist of gas originally ejected by the progenitor as a stellar wind or deposited by binary interaction. The high mass-loss rate and short ejection timescale can be achieved in the final stages of stellar evolution by several mechanisms: 1. a powerful outflow driven by super-Eddington wave energy deposition during the last few years before explosion (Quataert & Shiode 2012); 2. explosive mass ejection due to violent silicon flashes within a few weeks before the explosion of low-mass helium stars (Woosley 2019); 3. nonconservative case BB²² mass transfer in binary evolution of ultra-stripped stars (Tauris et al. 2015).

5.3. Stellar Evolution Pathways

Here we discuss possible evolution paths of SN2019dge’s progenitor.

We first consider the scenario in which SN2019dge comes from a progenitor more massive than $\sim 15 M_{\odot}$ in a binary system that loses its mass in case B mass transfer. Yoon et al. (2010) showed that subsequent wind mass loss is weak at subsolar metallicity of $Z \approx 0.004$ (similar to the $Z \approx 0.005$ calculated in Appendix C), such that the final mass of the primary at the time of core-collapse will be higher than $3.8 M_{\odot}$. This will lead to $M_{\text{ej}} \gtrsim 2.3 M_{\odot}$, assuming that the explosion forms a neutron star of $1.5 M_{\odot}$. This inferred ejecta mass is much higher than that observed ($M_{\text{ej}} \sim 0.3 M_{\odot}$), so this scenario is not favored.

We next consider the possibility that the primary has an initial mass $M_1 \lesssim 15 M_{\odot}$. In many binary configurations, the primary will be stripped of its hydrogen envelope during case B mass transfer, which could be either stable or unstable. The fairly low-mass ($M \lesssim 4 M_{\odot}$) primary helium star will expand after core helium depletion, followed by case BB mass transfer, which strips much of its helium envelope. Model 3 of

Yoon et al. (2010) and a few of the models from Table 1 of Tauris et al. (2015) are examples of systems whose evolution may be similar to the progenitor of SN2019dge, whose initial mass as a helium star was likely $M_{\text{He}} \sim 3 M_{\odot}$. Zapartas et al. (2017) performed population synthesis simulations, showing that for the pre-SN helium star to be stripped to a final mass $\lesssim 2 M_{\odot}$, a relatively wide range of companion mass is possible. So, the nature of the companion star remains unclear, and both main-sequence stars and compact objects are possible. What is clear is that case BB mass transfer was stable in this system, because the post-common envelope orbital separation of unstable case BB mass transfer would be much smaller than the inferred radius of the progenitor of SN2019dge (Laplace et al. 2020).

The final mass of the helium envelope depends on the initial mass of the helium star and the orbital period of the compact binary. To reconcile with the ejecta mass observed in SN2019dge, we expect a small final envelope mass ($\lesssim 0.3 M_{\odot}$) but large enough for optical helium features to be observed in the SN explosion ($\gtrsim 0.06 M_{\odot}$, Hachinger et al. 2012). This can be achieved in a system in which the progenitor is a helium star in a compact binary with $P_{\text{orb}} \gtrsim 0.2$ days at the start of the helium burning phase (Tauris et al. 2015). However, the large inferred radius of the progenitor requires an orbital separation $a \gtrsim 200 R_{\odot}$, implying an orbital period $P_{\text{orb}} \gtrsim 100$ d at the time of explosion, depending on the companion mass. We note that the large inferred radius of the progenitor is near the maximum photospheric radius reached by low-mass $M \lesssim 3 M_{\odot}$ helium stars (Kleiser et al. 2018a; Woosley 2019; Laplace et al. 2020), potentially challenging the assertion that case BB mass transfer has occurred. However, exploding stars without case BB mass loss retain significantly larger ejecta masses than our constraints for SN2019dge (Tauris et al. 2015; Woosley 2019), producing light curves that rise and fade too slowly (Kleiser et al. 2018a).

5.4. Comparison with Other Ultra-stripped SN Candidates

In addition to SN2019dge and iPTF14gqr, we search the literature for other subluminescent fast-evolving hydrogen-poor SNe whose light curves can potentially be well fitted by an early-time SCE component and a radioactivity-powered second peak with small M_{ej} . We recover iPTFF16hgs (De et al. 2018b) and SN2018lqo (De et al. 2020a) as ultra-stripped SN candidates. Here we apply our modeling approach described in Sections 4.1 and 4.3 to iPTF16hgs and SN2018lqo to distill the physical parameters of these two events. We show the results in Table 3. The ejecta masses of iPTF16hgs and SN2018lqo are greater than that in SN2019dge and iPTF14gqr by a factor of ~ 3 , and fall inside the range of M_{ej} expected in explosions of a helium star orbiting a compact object, but are at the upper side of the boundaries (Tauris et al. 2015).

A full discussion of the progenitors of iPTF16hgs and SN2018lqo is beyond the scope of this paper. Here we refer to a recent study conducted by De et al. (2020a), which classified these two objects into the “green Ca-Ib” subclass in the Ca-rich SNe category. This class of objects is spectroscopically similar to SNe Ib at maximum light, and does not exhibit line-blanketed continua at $\sim 3500\text{--}5500 \text{ \AA}$. De et al. (2020a) proposed that pure helium-shell detonations or deflagrations can explain their photometric and spectroscopic properties. Although it has been suggested that the existence of early first peak can distinguish ultra-stripped SNe from other Ca-rich transients arising from helium detonation on the surface of

²² In case BB mass transfer, Roche-lobe overflow happens after core helium exhaustion, but before carbon ignition.

Table 3

Model Parameters for Hydrogen-poor Subluminous Fast-evolving SNe where the Bolometric Light Curve Can Be Fitted with a Shock Cooling Powered Component and a Radioactivity-powered Component

Name	v_{ej} (km s^{-1})	$\tau_{m,A82}$ (d)	$M_{ej,A82}$ (M_{\odot})	$M_{Ni,A82}$ ($10^{-2} M_{\odot}$)	$M_{ej,KK19}$ (M_{\odot})	$M_{Ni,KK19}$ ($10^{-2} M_{\odot}$)	R_{ext} (10^{13} cm)	M_{ext} ($10^{-2} M_{\odot}$)
iPTF14gqr	10,000	$4.63^{+0.19}_{-0.20}$	$0.24^{+0.02}_{-0.02}$	$8.14^{+0.14}_{-0.15}$	0.24	8.57	$6.09^{+8.73}_{-3.18}$	$2.59^{+0.46}_{-0.34}$
iPTF16hgs	10,000	$12.32^{+0.99}_{-0.97}$	$1.68^{+0.28}_{-0.25}$	$2.51^{+0.20}_{-0.22}$	0.83	2.30	$2.45^{+14.08}_{-1.80}$	$9.27^{+3.40}_{-2.48}$
SN2018lqo	8250	$9.71^{+0.52}_{-0.37}$	$0.86^{+0.09}_{-0.06}$	$2.75^{+0.09}_{-0.07}$	0.63	3.08	$0.77^{+3.63}_{-0.51}$	$7.30^{+8.14}_{-4.06}$
SN2019dge	8000	$6.53^{+0.18}_{-0.17}$	$0.38^{+0.02}_{-0.02}$	$1.57^{+0.04}_{-0.03}$	0.33	1.69	$1.19^{+0.06}_{-0.05}$	$9.71^{+0.28}_{-0.27}$

Note. Model parameters with the subscripts of “A82” and “KK19” refer to radioactivity-powered light curve models of Arnett (1982) (see Appendix B.3) and Khatami & Kasen (2019), respectively. Reference: iPTF14gqr (De et al. 2018c), iPTF16hgs (De et al. 2018b), SN2018lqo (De et al. 2020a), SN2019dge (this work).

white dwarfs (Nakaoka et al. 2020), the early-time peak might also be caused by radioactive decay from short-lived isotopes in the outermost ejecta (De et al. 2020a). For example, the double-peaked Ca-rich transient SN2018lqo occurs in an elliptical galaxy, which is not expected to be the host for ultra-stripped SNe.

Although we include only hydrogen-poor events in this comparison, we note that SN2019ehk, a Ca-rich transient that exhibits flash-ionized hydrogen in its early-time spectra (Jacobson-Galán et al. 2020) as well as possible hydrogen photospheric features (De et al. 2020a), has also been suggested to be an ultra-stripped CCSN (Nakaoka et al. 2020). If both iPTF16hgs and SN2019ehk are bona fide ultra-stripped SNe, there might exist a continuum of ejecta mass, from normal stripped envelope SNe ($1 M_{\odot} \lesssim M_{ej} \lesssim 5 M_{\odot}$), to a higher degree of stripping in the progenitors of SN2019ehk and iPTF16hgs ($0.5 M_{\odot} \lesssim M_{ej} \lesssim 1 M_{\odot}$), to a more extreme degree of stripping seen in SN2019dge ($M_{ej} \sim 0.3 M_{\odot}$), to the most extreme stripping seen in iPTF14gqr ($M_{ej} \sim 0.2 M_{\odot}$). The remaining amount of helium, the companion mass, and final orbital separation might become smaller along this sequence.

6. Rates

As progenitors of compact neutron star binaries, the volumetric rates of ultra-stripped SNe have implications for our understanding of the evolutionary pathways leading to these systems and the gravitational waves detected by existing and upcoming facilities such as LIGO/VIRGO (Abbott et al. 2017a).

Based on population synthesis calculation, Tauris et al. (2015) estimate that the volumetric rates of ultra-stripped SNe should be $\sim 0.1\%$ – 1% of the rate of Core-collapse SNe. Using the properties of the promising ultra-stripped SN iPTF14gqr (De et al. 2018c), Hijikawa et al. (2019) estimate the volumetric rates of iPTF14gqr-like ultra-stripped SNe to be $\sim 2 \times 10^{-7} \text{Mpc}^{-3} \text{yr}^{-1}$, or $\sim 0.2\%$ of the local CCSNe rate (Li et al. 2011a). However, because existing ultra-stripped SN candidates were found outside of systematic SN classification efforts, observationally constraining the rates of ultra-stripped SNe has not been possible thus far.

6.1. Simple Estimation

6.1.1. Using the BTS Sample

SN2019dge was followed up as a part of the ZTF Bright Transient Survey (BTS, Fremling et al. 2020), which aims to spectroscopically classify all extragalactic transients in ZTF brighter than 18.5 mag at peak. Because BTS reads from only the ZTF public alert stream (highlighted with a greater marker

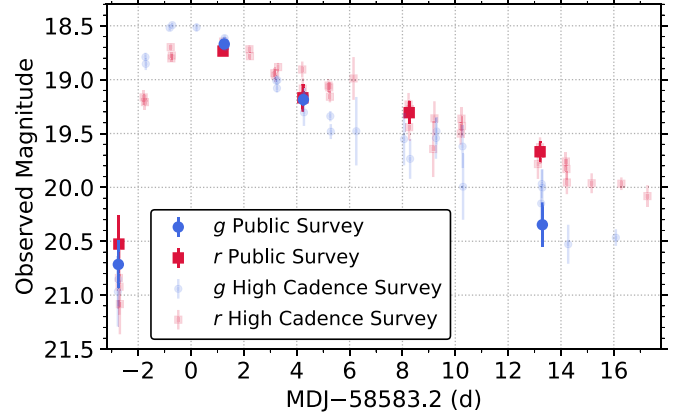


Figure 13. Un-binned P48 light curve of SN2019dge. We highlight observations obtained in the public Northern Sky Survey in a greater marker size and high-opacity colors, whereas observations obtained in the high-cadence survey are shown in semi-transparent.

size in Figure 13), SN2019dge peaks between 18.5 and 19.0 mag in the BTS sample. Thanks to the relatively high spectroscopic completeness ($\approx 89\%$) at the brightness limit of 19.0 mag, we can directly place constraints on the rates of 19dge-like ultra-stripped SNe using the BTS sample.

SN2019dge peaked at an absolute magnitude of -16.44 mag in g band. At the BTS peak brightness limit of 19.0 mag, objects similar to SN2019dge would be detectable out to 123 Mpc. Thus, taking only the local 123 Mpc volume within redshift of $z = 0.028$, we compare the number of CCSNe brighter than 19.0 mag at peak that were found in the BTS experiment in its first 12 months of operations (between 2018 June 1 and 2019 June 1). In this time period, BTS classified a total of 116 CCSNe in this volume. As such, the detection of one object in this sample constrains the rate of ultra-stripped SNe to be $\sim 0.86\%$ of the CCSNe rate brighter than $M = -16.44$ mag in this volume.

Taking the observed luminosity function of CCSNe in the local universe (Li et al. 2011b), we find that $\approx 50\%$ of CCSNe are fainter than $M = -16.44$ mag. The luminosity function corrected rate of 19dge-like events is then $\sim 0.43\%$ of the local CCSNe rate. The inferred rate is consistent with that estimated in Tauris et al. (2015), but higher than that inferred for iPTF14gqr-like events (Hijikawa et al. 2019). Adopting the CCSNe volumetric rate of $0.7 \times 10^{-4} \text{Mpc}^{-3} \text{yr}^{-1}$ (Li et al. 2011a), the volumetric rate of 19dge-like ultra-stripped SNe rate is $\sim 300 \text{Gpc}^{-3} \text{yr}^{-1}$. This rate estimation is only a lower limit, because the fast photometric evolution of objects similar to SN2019dge can be easily missed due to the slower 3 days’ cadence of the ZTF public survey.

6.1.2. Using the CLU sample

The ZTF team also conducts a campaign to spectroscopically classify all SNe within 200 Mpc by filtering transients occurring in galaxies with previously known redshifts within $z \leq 0.05$ in the Census of the Local Universe (CLU) catalog (De et al. 2020a). Hereafter we refer to this experiment as CLU. The spectroscopic completeness of transients in the CLU sample that had at least one detection brighter than 20 mag is 89%. Because CLU reads from the whole ZTF alert stream (e.g., all data points shown in Figure 13), the higher-cadence sub-surveys allow it to better characterize fast-evolving SNe. However, the uncertainty in this experiment is the incompleteness of the input galaxy catalog. The redshift completeness fraction (RCF) is $\approx 80\%$ at the lowest redshifts and decreases to $\approx 50\%$ at $z = 0.05$, as measured by the BTS experiment (Fremling et al. 2020).

At the CLU peak brightness limit of 20.0 mag, objects similar to SN2019dge would be detectable out to 195 Mpc. Between 2018 June 1 and 2019 June 1, CLU classified a total of 273 CCSNe in this volume, whereas no good ultra-stripped SN candidates have been identified. We place an upper limit of ultra-stripped SNe rate to be $\sim 5100 \text{ Gpc}^{-3} \text{ yr}^{-1}$ following the simple calculation described in Section 6.1.1. However, it is also susceptible to the fast evolution of 19dge-like SNe being missed by the observation gaps. In Section 6.2 we attempt to place robust estimates of 19dge-like ultra-stripped SNe rate by running simulated surveys with the ZTF cadence.

6.2. Estimation Based on Survey Simulations

We utilize `simsurvey` (Feindt et al. 2019), a python package designed for assessing the rates of transient discovery in surveys like ZTF. To simulate the expected yield of a specific type of transient given a volumetric rate, `simsurvey` requires three inputs: (1) A survey schedule. We use the actual ZTF observing history in g and r band between 2018 June 1 and 2019 June 1 in any of the public or collaboration surveys as the input survey plan. (2) A transient model. We construct a light-curve template of SN2019dge (see details in Appendix B.4). Using the template, we generate a `TimeSeriesSource` model in the `sncosmo` package (Barbary et al. 2016). (3) A function to sample the transient model parameters. Transients are injected out to a redshift of $z = 0.044$, because objects further out are not expected to peak brighter than 20.0 mag.

We examine the expected number of detected 19dge-like SNe for a range of input rates. For each input rate, we perform 300 simulations of the ZTF observing plan. To select transient candidates that would have passed the selection criteria of the BTS or CLU experiment and been flagged as an object with photometric properties consistent with being a 19dge-like ultra-stripped SN, we apply cuts on the simulated light curves as described below.

For the BTS filter, we use only public survey pointings, and reject SNe at low Galactic latitudes ($|b| \leq 7^\circ$) to be consistent with the BTS experiment (Fremling et al. 2020). In either the g - or r -band light curve, we identify peak light as the brightest detection in the simulated light curve, and require the following:

1. peak magnitude < 19.0 mag

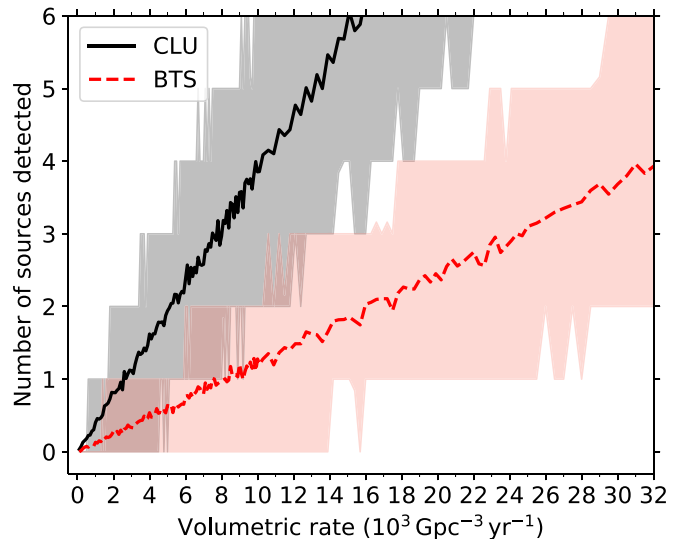


Figure 14. The number of sources passing criteria (described in text) as a function of the input volumetric rate, in both the BTS and CLU experiments. The lines show the mean of the 300 simulations, and the shaded boundaries indicate the 16th and 84th percentiles.

2. within 4.1 days before peak, there must be at least one detection or one upper limit deeper than 1.5 mag below peak
3. within 15 days after peak, there must be at least three detections, and the measured decline rate must be greater than $0.07 \text{ mag days}^{-1}$.

Criterion (ii) is set to require that the fast rise of the light curve can be recognized from the observation. This is essential because if we discover SN2019dge only at the radioactive tail, we will probably classify it as a low-velocity SN Ib. Criterion (iii) is made to ensure that the rapid decline of the light curve can be captured, such that the small ejecta mass can be inferred.

For the CLU filter, we use all ZTF pointings, and require that in either the g - or r -band light curve:

1. peak magnitude < 20.0 mag
2. the light curve must satisfy at least one of the following criteria: (1) within 4.1 days before peak, there must be at least one detection or one upper limit deeper than 1.5 mag below peak; (2) within 2.5 days before peak, there must be at least one detection deeper than 0.75 mag below peak
3. same as criterion (iii) applied in the BTS filter.

We apply the above criteria to the actual observations of CCSNe in the BTS and CLU sample. We identify one other SN—ZTF18abwkrbl (SN2018gix)—that passes our criteria. However, ZTF18abwkrbl is a SN IIB that clearly shows hydrogen in the spectra, and can therefore be excluded as an ultra-stripped SN candidate (Tauris et al. 2015).

In Figure 14, we show the number of transients that pass our selection criteria as a function of the input volumetric rate. The solid line and shaded region indicate the mean and 68% credible region of the 300 simulations. In the actual BTS experiment, there was only *one* detected ultra-stripped SN. Therefore, we consider the range of volumetric rate where *one* falls within the shaded red region as a constraint on the rate of 19dge-like ultra-stripped SNe. This gives R_{19dge} in the range of $1400\text{--}28,000 \text{ Gpc}^{-3} \text{ yr}^{-1}$.

Using the fact that there were *zero* ultra-stripped SN detected in the actual CLU experiment, the gray shaded region in

Figure 14 might suggest $R_{19dge} \lesssim 4500 \text{ Gpc}^{-3} \text{ yr}^{-1}$. However, this upper limit needs to be corrected for offset distribution and galaxy catalog incompleteness. First of all, as discussed in De et al. (2020a), the CLU experiment is restricted to transients coincident within $100''$ of the host-galaxy nuclei. SN2019dge and iPTF14gqr are $0''.5$ and $24''$ from their host galaxies (all within $100''$). Although a large sample of ultra-stripped SNe is needed to examine the host offset distribution of this class of objects, the fact that they arise from massive binary evolution suggest that the correction due to this factor should be small. Second, the incompleteness of the input galaxy catalog possibly leads to an underestimation of ultra-stripped SNe rate by a factor of 55%–80%, as indicated by the RCF. We adjust for such an incompleteness by increasing the upper limit from 4500 to $8200 \text{ Gpc}^{-3} \text{ yr}^{-1}$.

Combining results from the BTS and CLU experiments, we derive a 19dge-like ultra-stripped SNe rate of $1400\text{--}8200 \text{ Gpc}^{-3} \text{ yr}^{-1}$, corresponding to 2%–12% of CCSNe rate.

6.3. Effects of Different Envelope Masses and Radii

Given the low mass of ultra-stripped progenitors, we expect to see SCE from the inflated pre-explosion star, as has been clearly seen in the case of iPTF14gqr and SN2019dge in the fast early-time evolution and blue colors of the optical light curve. As is shown by Nakar & Piro (2014, Figure 2), rise time of the SCE is determined by mass of the extended material M_{ext} , while the peak luminosity is mainly modulated by R_{ext} . We demonstrate this dependence in Figure 15. We simulate SCE with the P20 model by varying M_{ext} and R_{ext} , and at the same time setting $E_{\text{ext}} = 5.30 \times 10^{49} \text{ erg}$ (the value found in SN2019dge).

In the upper panel, t_{rise} is defined in the same way as in Section 3.1.1 (rise time from half-max to max). The rising part of the cooling light curve can be captured by a three-day, two-day, and one-day cadence optical survey at $M_{\text{ext}} \gtrsim 0.14 M_{\odot}$, $\gtrsim 0.07 M_{\odot}$, and $\gtrsim 0.03 M_{\odot}$, respectively. Transients with $M_{\text{ext}} \gtrsim 0.15 M_{\odot}$ will not pass our selection criteria in Section 6.2. In the bottom panel, we show the expected absolute luminosity at peak of the g -band cooling light curve. As is readily shown, for ultra-stripped progenitors with an extended radius $\lesssim 10^{13} \text{ cm}$, a survey like ZTF is only sensitive to objects in the local universe ($\lesssim 100\text{--}150 \text{ Mpc}$) for the subsequent evolution of the light curve to be well characterized. Taken together, we conclude that our estimation of the ultra-stripped SNe rate does not include ultra-stripped progenitors with $M_{\text{ext}} \gtrsim 0.15 M_{\odot}$ or $R_{\text{ext}} \lesssim 10^{13} \text{ cm}$.

6.4. Discussion

If the companion of the pre-explosion helium star is a low-mass main-sequence star, a white dwarf, or a black hole, SN2019dge will not be the progenitor of a double neutron star system, and thus the inferred R_{19dge} is not connected with R_{DNS} . Even in the case that the companion is a neutron star, if the forming DNS binary has orbital periods more than ~ 1 days, it will not merge within the age of the universe (Tauris et al. 2015). Therefore, the above estimation of the ultra-stripped SNe rate should provide an upper limit to the local coalescence rate density (R_{DNS}) of double neutron stars not formed via dynamical capture in a globular cluster (East & Pretorius 2012; Andrews & Mandel 2019).

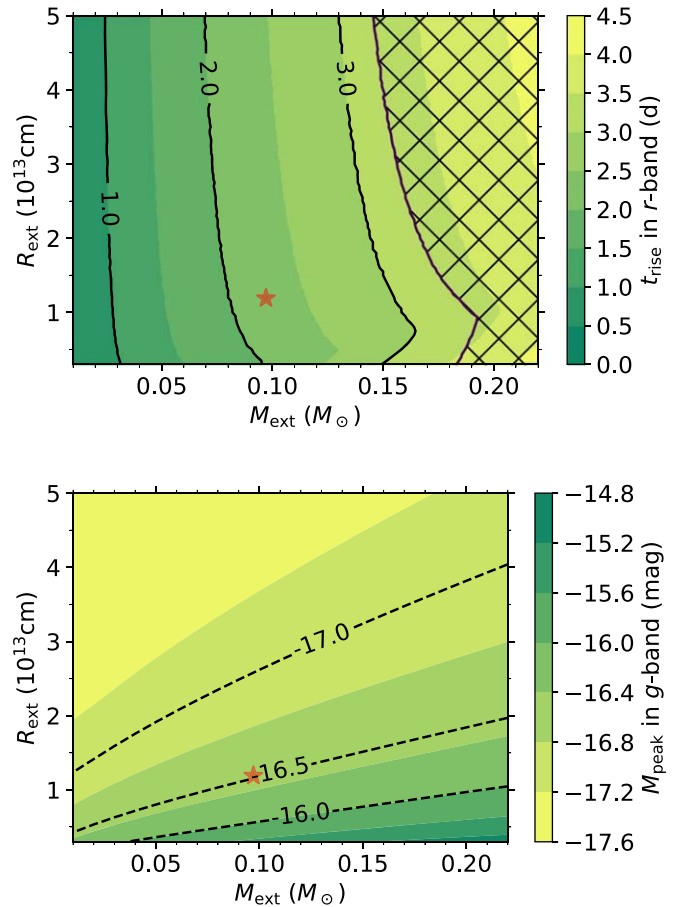


Figure 15. Expected r -band rise time (upper panel) and g -band peak absolute luminosity (bottom panel) as a function of shock cooling model parameters R_{ext} and M_{ext} . The position of SN2019dge is indicated by the red asterisks. In the upper panel, parameter space that could not pass our criteria of “rise from 1.5 mag below peak to peak in less than 4.1 days” (Section 6.2) is indicated by the hatched region.

7. Conclusion

In this paper we have presented the discovery, observation, and modeling of the transient SN2019dge. We summarize the main characteristics of this object below:

1. Peak absolute magnitudes are $M_{g,\text{peak}} \approx -16.5 \text{ mag}$ and $M_{r,\text{peak}} \approx -16.3 \text{ mag}$. In r band, rise time (half-max to max) is 2.0 days, and decay time (max to half-max) is 8.6 days. SN2019dge is one of the most rapidly rising subluminous SNe I discovered to date.
2. Early-time spectra show a blue continuum and flash He II features that indicate a high mass-loss rate of $\gtrsim 10^{-4} M_{\odot} \text{ yr}^{-1}$.
3. Photospheric spectra indicate helium-rich ejecta, and the prominent NUV Mg II emission suggests interaction between SN ejecta and CSM.
4. Late-time spectra show signatures of interaction with helium-rich CSM, similar to that observed in Type Ibn SNe.
5. The bolometric light curve of SN2019dge peaks at $\sim 5 \times 10^{42} \text{ erg s}^{-1}$, and can be explained by a combination of two components. The first component is consistent with shock cooling from an envelope of $\sim 0.1 M_{\odot}$ located $\sim 1.2 \times 10^{13} \text{ cm}$ ($170 R_{\odot}$) from the progenitor. The second component is powered by $\sim 0.017 M_{\odot}$ of ^{56}Ni .

6. We estimate the ejecta mass and kinetic energy of SN2019dge to be $\sim 0.33 M_{\odot}$ and $\sim 1.3 \times 10^{50}$ erg, respectively.

We interpret SN2019dge as a helium-rich ultra-stripped envelope SN.

Based on the one event, we estimate the rate density of 19dge-like ultra-stripped SNe (with $M_{\text{ext}} \lesssim 0.15 M_{\odot}$ and $R_{\text{ext}} \gtrsim 10^{13}$ cm) to be $1400\text{--}8200 \text{ Gpc}^{-3} \text{ yr}^{-1}$. This can be compared to the merger rate of DNS systems not formed via dynamical capture. The first detection of gravitational waves from the merging DNS binary GW170817 gave $R_{\text{DNS}} = 320\text{--}4740 \text{ Gpc}^{-3} \text{ yr}^{-1}$ (Abbott et al. 2017a). Detection of GW190425 provides an update of $R_{\text{DNS}} = 250\text{--}2810 \text{ Gpc}^{-3} \text{ yr}^{-1}$ (Abbott et al. 2020). Based on an archival search for EM170817-like transients (known as “kilonovae” or “macronovae”) in the PTF database, Kasliwal et al. (2017) reported an upper limit on the rate of $800 \text{ Gpc}^{-3} \text{ yr}^{-1}$, which might be doubled if the typical kilonova is 50% fainter than EM170817.

It is important to compare ultra-stripped SNe rate and R_{DNS} constrained by future GW observations. If the former is smaller than the latter, it will provide evidence for the dynamical formation channel to be the major path for forming DNS systems. A better constraint of ultra-stripped SNe rate is also essential in our understanding of the final stages of helium star evolution in binary systems. As such, further systematic searches for ultra-stripped SNe are required to reduce the large uncertainties of the current estimation. Moving forward, the discovery of ultra-stripped SNe will still rely on high-cadence wide-field experiments such as ZTF. In particular, the upcoming ZTF-II, with a two-day cadence all sky survey, coupled with higher-cadence boutique experiments, is well positioned to carry out this task.

We thank Takashi Moriya, Thomas Tauris, David Khatami, Dan Kasen, Sterl Phinney, and Wenbin Lu for valuable discussions during this work. We thank Lin Yan for sharing spectra of SN1993J and Gaia16apd. Y.Y. thanks the instructors and organizers of the GROWTH summer school for teaching techniques in time-domain data analysis. This study made use of the open supernova catalog (Guillochon et al. 2017).

C.F. gratefully acknowledges support of his research by the Heising-Simons Foundation (#2018-0907).

This work was supported by the GROWTH project funded by the National Science Foundation under PIRE grant No. 1545949.

This work is based on observations obtained with the Samuel Oschin Telescope 48 inch and the 60 inch Telescope at the

Palomar Observatory as part of the Zwicky Transient Facility project. ZTF is supported by the National Science Foundation under grant No. AST-1440341 and a collaboration including Caltech, IPAC, the Weizmann Institute for Science, the Oskar Klein Center at Stockholm University, the University of Maryland, the University of Washington, Deutsches Elektronen-Synchrotron and Humboldt University, Los Alamos National Laboratories, the TANGO Consortium of Taiwan, the University of Wisconsin at Milwaukee, and Lawrence Berkeley National Laboratories. Operations are conducted by COO, IPAC, and UW.

Software: astropy (Astropy Collaboration et al. 2013), corner (Foreman-Mackey 2016), CIGALE (Boquien et al. 2019), emcee (Foreman-Mackey et al. 2013), LAMBDAR (Wright et al. 2016), Lpipe (Perley 2019), matplotlib (Hunter 2007), pandas (McKinney 2010), pyneb (Luridiana et al. 2015), pyraf-dbsp (Bellm & Sesar 2016), scipy (Virtanen et al. 2020), simsurvey (Feindt et al. 2019), snocosmo (Barbary et al. 2016), ztfquery (Rigault 2018).

Appendix A UV and Optical Data

The full set of photometry of SN2019dge is listed in Table A1.

Table A1
Optical and UV Photometry for SN2019dge

Date (MJD)	Instrument	Filter	m	σ_m
58582.1544	LT+IOO	g	18.590	0.010
58582.1552	LT+IOO	r	18.840	0.020
58582.1575	LT+IOO	i	19.110	0.020
58582.1583	LT+IOO	z	19.280	0.070
58584.2341	LT+IOO	u	18.570	0.020
58580.4421	P48+ZTF	g	20.828	0.148
58580.4842	P48+ZTF	r	20.891	0.139
58582.8289	Swift+UVOT	B	18.606	0.193
58582.8280	Swift+UVOT	U	18.289	0.113
58582.8346	Swift+UVOT	$UVM2$	18.550	0.068
58582.8261	Swift+UVOT	$UVW1$	18.685	0.108
58582.8299	Swift+UVOT	$UVW2$	18.802	0.103
58582.8337	Swift+UVOT	V	18.679	0.404

Note. m and σ_m are observed magnitude (without extinction correction) in AB system. A machine-readable table of all 120 photometric data points will be made available online.

(This table is available in its entirety in machine-readable form.)

Appendix B Modeling of SN2019dge

B.1. Modeling the Physical Evolution

To model the multiband light curve with a blackbody function, we utilized the Monte Carlo Markov Chain (MCMC) simulations with `emcee` (Foreman-Mackey et al. 2013). We test the performance of three types of model priors for the blackbody radius (R_{bb}) and temperature (T_{bb}): (i) T_{bb} and R_{bb} are uniformly distributed in the range of $[10^3, 10^7]$ K and $[10, 10^6] R_{\odot}$, respectively (ii) the two parameters are logarithmically and uniformly distributed in the same ranges (iii) the two parameters follow Jeffreys prior (Jeffreys 1946) in the same ranges.

Within the ensemble, we use 100 walkers, each of which is run until convergence or 100,000 steps, whichever comes first. The test for convergence follows steps outlined in Yao et al. (2019) and Miller et al. (2020). We adopt the 68% credible region (i.e., 16th and 84th percentiles of posterior probability distributions) as the model uncertainties quoted in Table B1.

We examine the fitting results under different choices of priors in Figure B1, which shows the posterior distribution of T_{bb} using data obtained on April 7 (top panels) and April 9 (bottom panels). Many early stages of SN evolution feature extremely high temperatures. At an epoch when both UV and optical data are available (April 9), the posterior does not depend on the particular choice of prior, and the model parameter can thus be well constrained. However, at our first detection epoch, for which only optical data are available (April 7), the posterior strongly depends on the prior. For a linearly flat prior, high numbers receive a lot of “weight,” making the “multi-peaks” shape posterior in the upper-left panel of Figure B1. Log prior and Jeffreys prior generally give similar results. In this study, we adopt results using log prior. However, we note that the choice of prior does not affect final estimates of maximum luminosity, or the model fits for shock cooling and ^{56}Ni decay.

In Figure B2 we show the photometry interpolated onto common epochs, and fit to a blackbody function to derive the photospheric evolution. The resulting evolution in bolometric luminosity, photospheric radius, and effective temperatures is listed in Table B1.

B.2. Modeling Early Light Curve

We use the P20 analytical expression for the shape of the early-time light curve in terms of M_{ext} , R_{ext} , and E_{ext} . Following P20, we adopt typical values of the density structure $n \approx 10$ and $\delta \approx 1.1$.

We fix $\kappa \approx 0.2 \text{ cm}^2 \text{ g}^{-1}$ as appropriate for a hydrogen-deficient ionized gas, and assign wide flat priors for all model parameters, as summarized in Table B2. We include only observations up to $\Delta t = 2$ d in the fitting. We found that this particular choice of $\Delta t = 2$ days instead of 1 days or 3 days in general does not affect the final inference for the model parameters. Figure B3 shows the corner plot of $\log R_{\text{ext}}$, $\log M_{\text{ext}}$, t_{exp} , and $E_{\text{ext},49}$.

The maximum a posteriori model is visualized by solid lines in Figure B4 color-coded in different filters. Nevertheless, the early evolution of the light curve is well captured by this model.

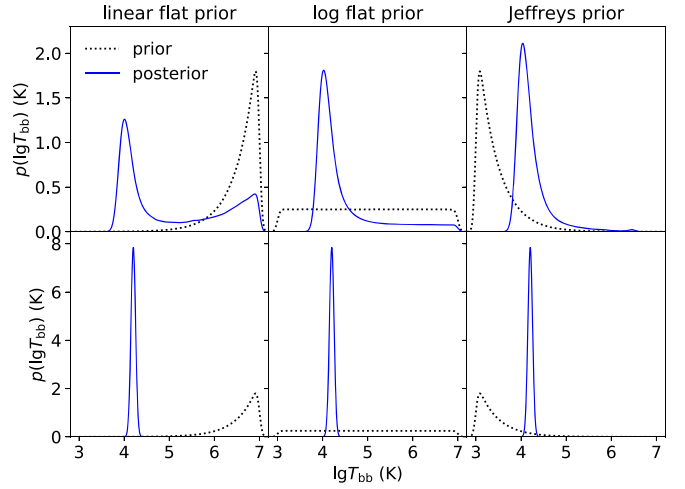


Figure B1. Posterior (solid lines) distribution of the blackbody temperature T_{bb} on April 7 (upper panels) and April 9 (bottom panels) using three different priors (dotted lines).

Table B1
Physical Evolution of SN2019dge from Blackbody Fits

Δt	$L (10^{41} \text{ erg s}^{-1})$	$R (10^3 R_{\odot})$	$T (10^3 \text{ K})$
-2.74	$2.98^{+578.84}_{-1.41}$	$1.45^{+1.14}_{-5.12}$	$14.21^{+101.35}_{-5.12}$
-1.72	$44.63^{+43.85}_{-15.84}$	$2.20^{+0.44}_{-0.46}$	$22.75^{+7.60}_{-4.14}$
-0.69	$26.96^{+0.92}_{-0.87}$	$3.50^{+0.07}_{-0.07}$	$15.90^{+0.28}_{-0.27}$
0.24	$22.87^{+0.62}_{-0.61}$	$4.46^{+0.08}_{-0.08}$	$13.51^{+0.21}_{-0.21}$
1.09	$17.50^{+0.40}_{-0.37}$	$4.89^{+0.10}_{-0.10}$	$12.07^{+0.19}_{-0.18}$
3.26	$8.34^{+0.22}_{-0.20}$	$7.26^{+0.46}_{-0.44}$	$8.23^{+0.31}_{-0.28}$
4.24	$7.29^{+0.26}_{-0.22}$	$7.38^{+0.88}_{-0.83}$	$7.88^{+0.54}_{-0.46}$
5.25	$6.10^{+0.16}_{-0.15}$	$8.77^{+0.78}_{-0.73}$	$6.92^{+0.33}_{-0.30}$
6.83	$6.18^{+0.63}_{-0.46}$	$7.09^{+1.01}_{-0.92}$	$7.72^{+0.75}_{-0.62}$
7.98	$5.29^{+0.24}_{-0.21}$	$8.00^{+0.75}_{-0.70}$	$6.99^{+0.39}_{-0.35}$
8.98	$5.49^{+0.44}_{-0.36}$	$6.79^{+0.94}_{-0.85}$	$7.66^{+0.65}_{-0.56}$
10.05	$4.55^{+0.37}_{-0.27}$	$7.42^{+1.03}_{-0.96}$	$6.99^{+0.63}_{-0.52}$
10.92	$4.49^{+0.64}_{-0.44}$	$6.63^{+1.25}_{-1.06}$	$7.37^{+0.93}_{-0.75}$
11.89	$4.04^{+0.24}_{-0.21}$	$7.42^{+0.83}_{-0.75}$	$6.79^{+0.45}_{-0.40}$
13.06	$3.34^{+0.10}_{-0.10}$	$7.52^{+0.69}_{-0.66}$	$6.43^{+0.32}_{-0.29}$
14.05	$3.08^{+0.10}_{-0.09}$	$7.05^{+0.63}_{-0.59}$	$6.51^{+0.32}_{-0.29}$
14.97	$2.82^{+0.15}_{-0.12}$	$7.30^{+1.21}_{-1.06}$	$6.25^{+0.57}_{-0.49}$
16.09	$2.45^{+0.09}_{-0.09}$	$6.17^{+0.59}_{-0.58}$	$6.56^{+0.33}_{-0.29}$
23.96	$1.02^{+0.07}_{-0.06}$	$5.47^{+1.23}_{-1.12}$	$5.59^{+0.74}_{-0.54}$
27.00	$0.72^{+0.08}_{-0.08}$	$4.08^{+1.26}_{-1.01}$	$5.93^{+0.91}_{-0.70}$
27.98	$0.78^{+0.07}_{-0.06}$	$5.73^{+1.68}_{-1.29}$	$5.10^{+0.68}_{-0.57}$
29.23	$0.83^{+0.11}_{-0.09}$	$4.76^{+2.47}_{-1.56}$	$5.64^{+1.23}_{-0.93}$
33.24	$1.09^{+0.16}_{-0.11}$	$6.99^{+2.47}_{-1.74}$	$5.02^{+0.65}_{-0.56}$

B.3. Modeling the Main Peak

For $^{56}\text{Ni} \rightarrow ^{56}\text{Co} \rightarrow ^{56}\text{Fe}$ decay powered explosions, the energy deposition rate is

$$\epsilon_{\text{rad}} = \epsilon_{\text{Ni},\gamma}(t) + \epsilon_{\text{Co},\gamma}(t) \quad (\text{B1})$$

$$\epsilon_{\text{Ni},\gamma}(t) = \epsilon_{\text{Ni}} e^{-t/\tau_{\text{Ni}}} \quad (\text{B2})$$

$$\epsilon_{\text{Co},\gamma}(t) = \epsilon_{\text{Co}} (e^{-t/\tau_{\text{Co}}} - e^{-t/\tau_{\text{Ni}}}) \quad (\text{B3})$$

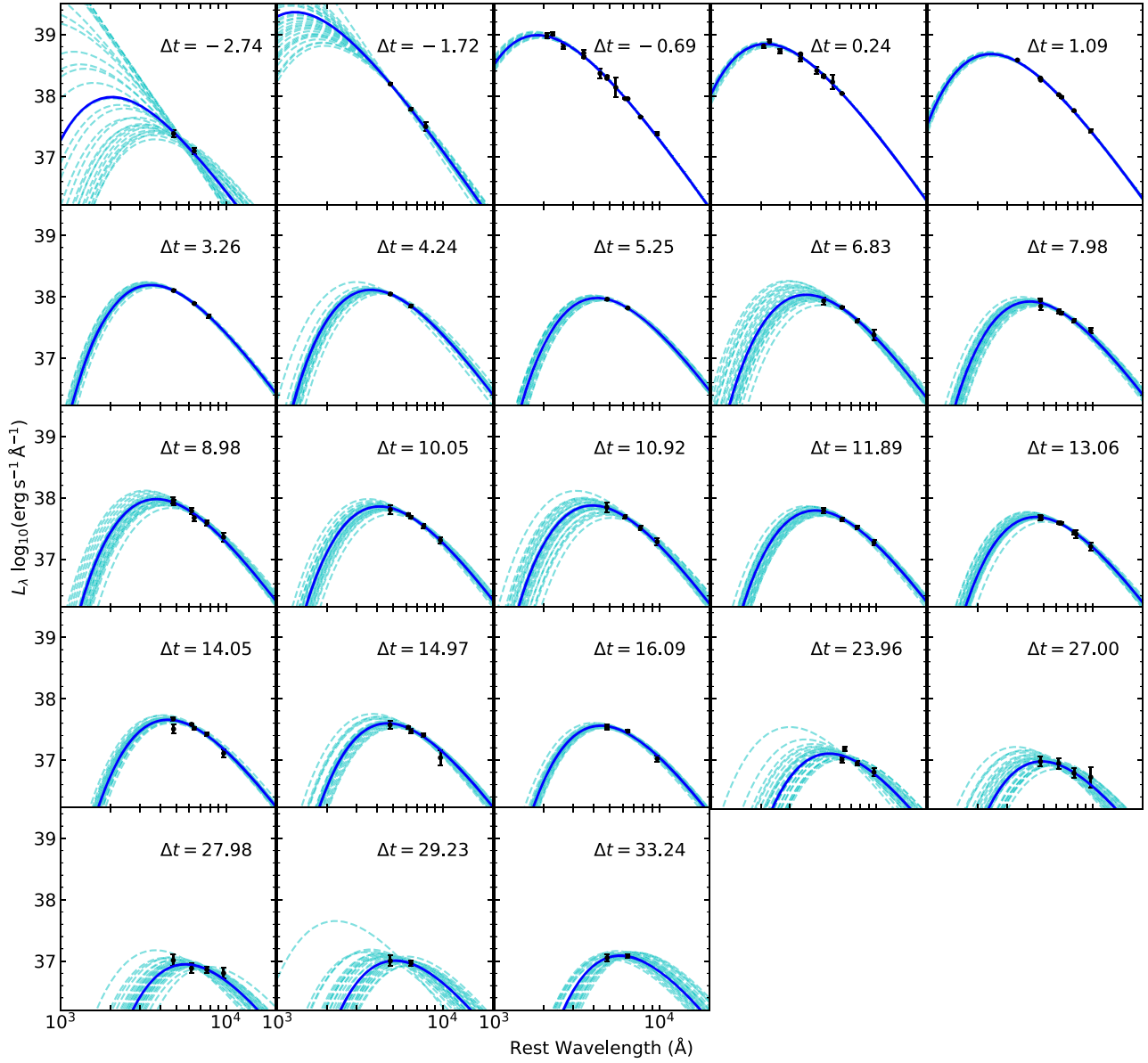


Figure B2. Black data points are Swift/UVOT and optical photometry of SN2019dge. Solid lines show model fits using estimated parameters, while 30 random draws from the MCMC posterior are shown with dashed lines.

Table B2
Shock Cooling Model Parameters θ and their Priors

θ	Description	Prior
$\log R_{\text{ext}}$	\log_{10} of extended material radius in cm	$\mathcal{U}(-5, 25)$
$\log M_{\text{ext}}$	\log_{10} of extended material mass in M_{\odot}	$\mathcal{U}(-4, 0)$
t_{exp}	explosion epoch in MJD relative to 58583.2	$\mathcal{U}(-8, -2.76)$
$E_{\text{ext},49}$	E_{ext} divided by 10^{49} erg	$\mathcal{U}(0.1, 100)$

where $\epsilon_{\text{Ni}} = 3.90 \times 10^{10} \text{ erg g}^{-1} \text{ s}^{-1}$, $\epsilon_{\text{Co}} = 6.78 \times 10^9 \text{ erg g}^{-1} \text{ s}^{-1}$, $\tau_{\text{Ni}} = 8.8 \text{ d}$, and $\tau_{\text{Co}} = 111.3 \text{ d}$ are the decay lifetimes of ^{56}Ni and ^{56}Co (Nadyozhin 1994). The effective heating rate is modified by the probability of thermalization, and thus $\epsilon_{\text{heat}} \leq \epsilon_{\text{rad}}$.

The bolometric light curve can be generally divided into the photospheric phase and the nebular phase. The photospheric phase can be modeled using equations given in Valenti et al. (2008, Appendix A), with modifications given by Lyman et al. (2016, Equation (3)),

$$\begin{aligned}
 L_{\text{phot}}(t) = & M_{\text{Ni}} e^{-x^2} \\
 & \times \left[(\epsilon_{\text{Ni}} - \epsilon_{\text{Co}}) \int_0^x (2ze^{-2zy+z^2}) dz \right. \\
 & \left. + \epsilon_{\text{Co}} \int_0^x (2ze^{-2zy+2zs+z^2}) dz \right]
 \end{aligned} \tag{B4}$$

where $x = t/\tau_{\text{m}}$, $y = \tau_{\text{m}}/(2\tau_{\text{Ni}})$,

$$s = \frac{\tau_{\text{m}}(\tau_{\text{Co}} - \tau_{\text{Ni}})}{2\tau_{\text{Co}}\tau_{\text{Ni}}}, \tag{B5}$$

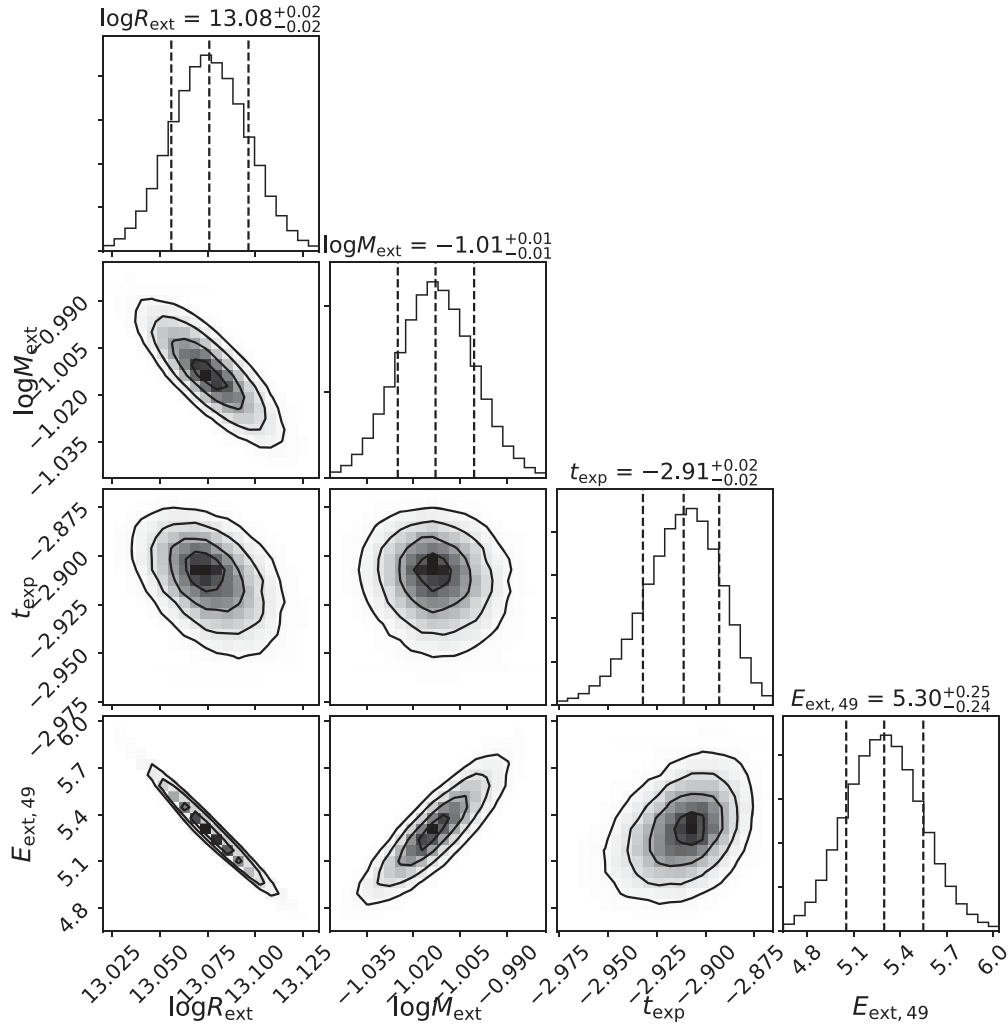


Figure B3. Corner plot showing the posterior constraints on $\log R_{\text{ext}}$, $\log M_{\text{ext}}$, t_{exp} , and $E_{\text{ext},49}$. Marginalized one-dimensional distributions are shown along the diagonal, along with the median estimate and the 68% credible region (shown with vertical dashed lines).

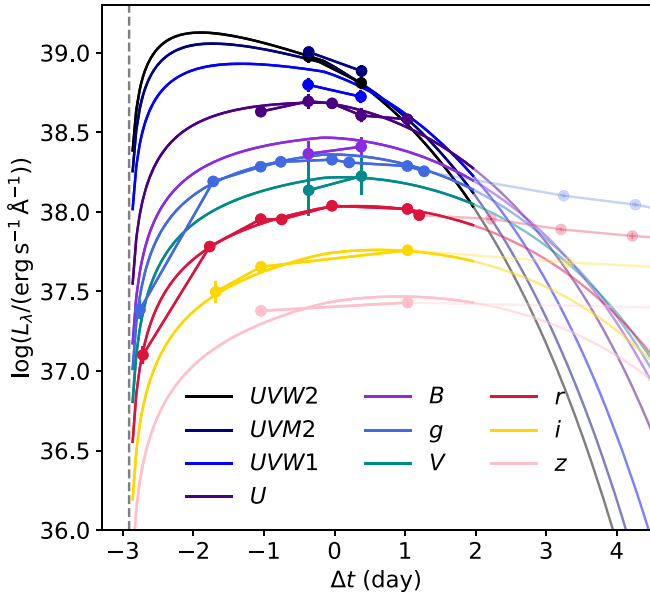


Figure B4. Cooling emission model fit to the early light curve of SN2019dge. Data excluded from the fitting are shown as transparent circles. The maximum a posteriori model is shown via solid lines. The vertical dashed line shows the median 1-D marginalized posterior value of t_{exp} .

$$\tau_m = \left(\frac{2\kappa_{\text{opt}} M_{\text{ej}}}{13.8c v_{\text{phot}}} \right)^{1/2} \quad (\text{B6})$$

In the nebular phase the SN ejecta becomes optically thin, such that the delay between the energy deposition from radioactivity and the optical radiation becomes shorter. The bolometric luminosity is then equal to the rate of energy deposition: $L_{\text{neb}}(t) = Q(t)$. At any given time, the energy deposition rate $Q(t)$ is Wheeler et al. (2015; Wygoda et al. 2019):

$$Q(t) \approx Q_\gamma(t)(1 - e^{-(t_0/t)^2}) \quad (\text{B7})$$

where $Q_\gamma(t) = M_{\text{Ni}} \epsilon_{\text{rad}}$ is the energy release rate of gamma-rays, and t_0 is the time at which the ejecta becomes optically thin to gamma-rays. Here the difference between the energy deposition rate of gamma-rays and positrons is neglected.

To fit the shock cooling subtracted bolometric light curve with a simple radioactive decay model, we do not divide the data into photospheric phase and nebular phase, but instead adopt the following formula for the whole light curve:

$$L(t) = L_{\text{phot}}(t)(1 - e^{-(t_0/t)^2}) \quad (\text{B8})$$

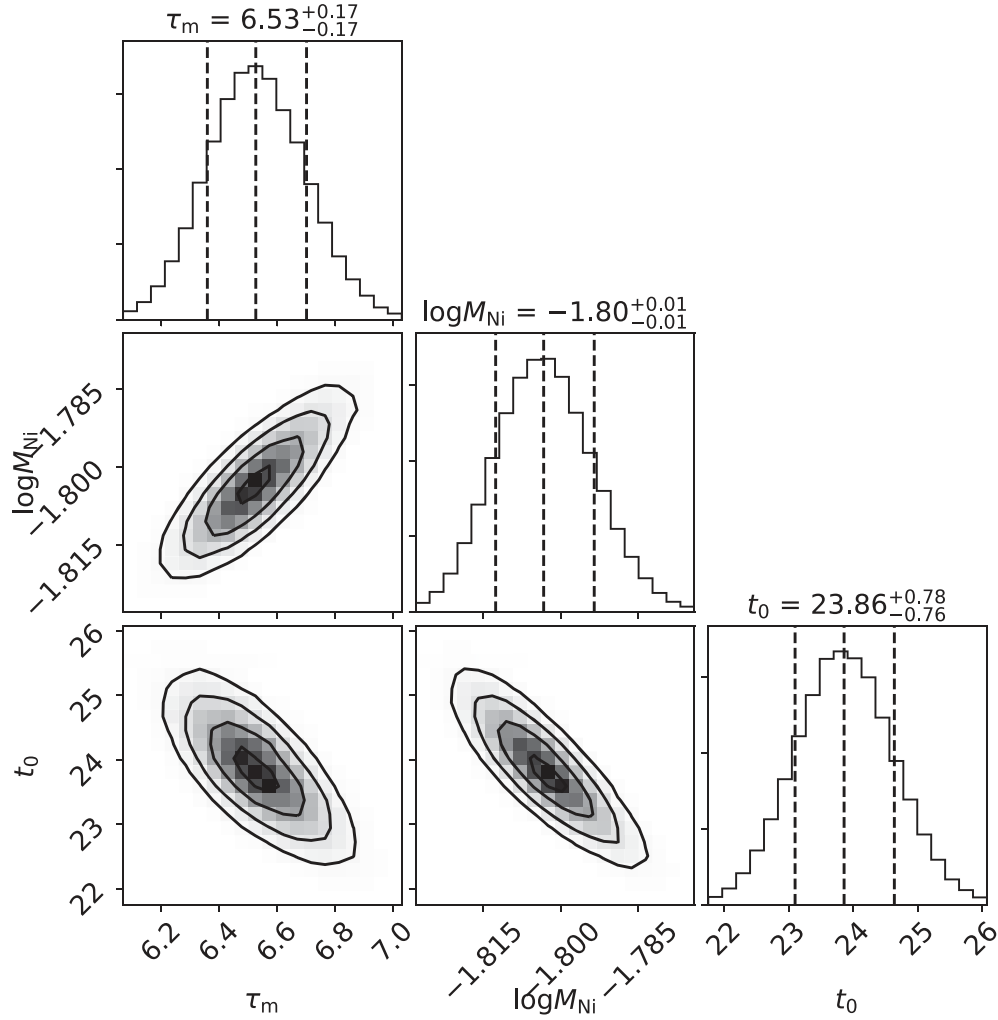


Figure B5. Corner plot showing the posterior constraints on τ_m , $\log M_{\text{Ni}}$, and t_0 .

Table B3
 ^{56}Ni Decay Model Parameters θ and Their Priors

θ	Description	Prior
τ_m	characteristic photon diffusion time in day	$\mathcal{U}(1, 20)$
$\log M_{\text{Ni}}$	\log_{10} of nickel mass in M_{\odot}	$\mathcal{U}(-4, 0)$
t_0	characteristic γ -ray escape time in day	$\mathcal{U}(20, 100)$

Priors of the model parameters are summarized in Table B3, and Figure B5 shows the corner plot of τ_m , $\log M_{\text{Ni}}$, and t_0 .

B.4. Generating a Light-curve Template for SN2019dge

To construct a template for SN2019dge in the ZTF g and r filters, we model the observed light curve by a Gaussian process. We denote the measurements as (\mathbf{x}, \mathbf{y}) , where \mathbf{x} is $\text{MJD} - 58583.2$, and \mathbf{y} is flux calculated as $10^{-0.4m} \times 10^8$ (m is magnitude). We choose a kernel in the form of Matern covariance function (Rasmussen 2003, Equation (4.17):

$$k_{3/2}(x, x') = A \left(1 + \frac{\sqrt{3}r}{l} \right) \exp \left(-\frac{\sqrt{3}r}{l} \right) \quad (\text{B9})$$

where $r = |x - x'|$. A and r in Equation (B9) are chosen to minimize the negative log likelihood function (see, e.g., Equation (2.43) of Rasmussen 2003).

We perform the fit from $x = -10$ d to $x = +40$ d, and the obtained templates are shown in Figure B6.

B.5. Constraints from Radio Upper Limits

Radio emission in SNe is produced by shock-accelerated electrons in the circumstellar material as they gyrate in the post-shock magnetic field when the shock freely expands. Should the CSM be formed by a pre-SN stellar wind, the radio synchrotron radiation can be used to probe the pre-explosion mass loss (Chevalier 1982). High-frequency ($\nu > 90$ GHz) bright ($\nu L_{\nu} \gtrsim 10^{40}$ erg s^{-1}) radio sources are often found to be associated with gamma-ray bursts (GRBs), tidal disruption events, and relativistic transients (see Figure 6 of Ho et al. 2019b). Among normal SNe Ibc, moderate submillimeter luminosity at $\sim 5 \times 10^{37}$ erg s^{-1} has been observed in SN1993J (Weiler et al. 2007) and SN2011dh (Horesh et al. 2013).

Our SMA observations constrain the submillimeter luminosity of SN2019dge to $\nu L_{\nu, 230\text{GHz}} < 5.3 \times 10^{39}$ erg s^{-1} and $\nu L_{\nu, 345\text{GHz}} < 3.0 \times 10^{40}$ erg s^{-1} . We place these upper limits in physical context using the synchrotron self-absorption model

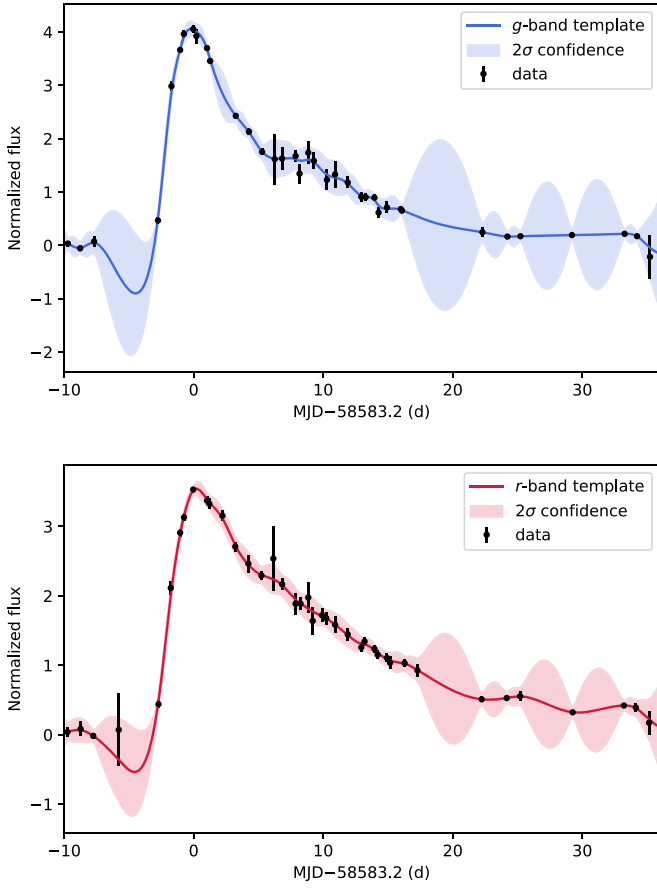


Figure B6. g - and r -band light-curve templates for SN2019dge obtained from Gaussian process fitting.

given by Chevalier (1998). The expected radio luminosities are computed at 230 and 345 GHz for two types of circumstellar environments—one with a wind density with the same parameterization as that adopted in Section 4.2, and the other with a constant-density environment ($\rho = \text{constant}$).

Adopting the explosion epoch found in Section 4.1, our SMA observations were obtained at 2.75 days after explosion. Given the early time of these observations, we consider constant shock velocities at $0.1\text{--}0.25c$, as found to be typical in SNe Ibc (Wellons et al. 2012). We assume an electron energy power-law index of $p = 3$, a volume-filling factor $f = 0.5$, and that the electrons and magnetic field in the post-shock region share constant fractions of the post-shock energy density, i.e., $\epsilon_e = \epsilon_B = 0.1$.

The expected radio luminosity predicted by the Chevalier model in the two environments at 230 GHz are shown in Figure B7 by the color maps, and the black contours indicate our 3σ limits. As can be seen, only small regions have expected

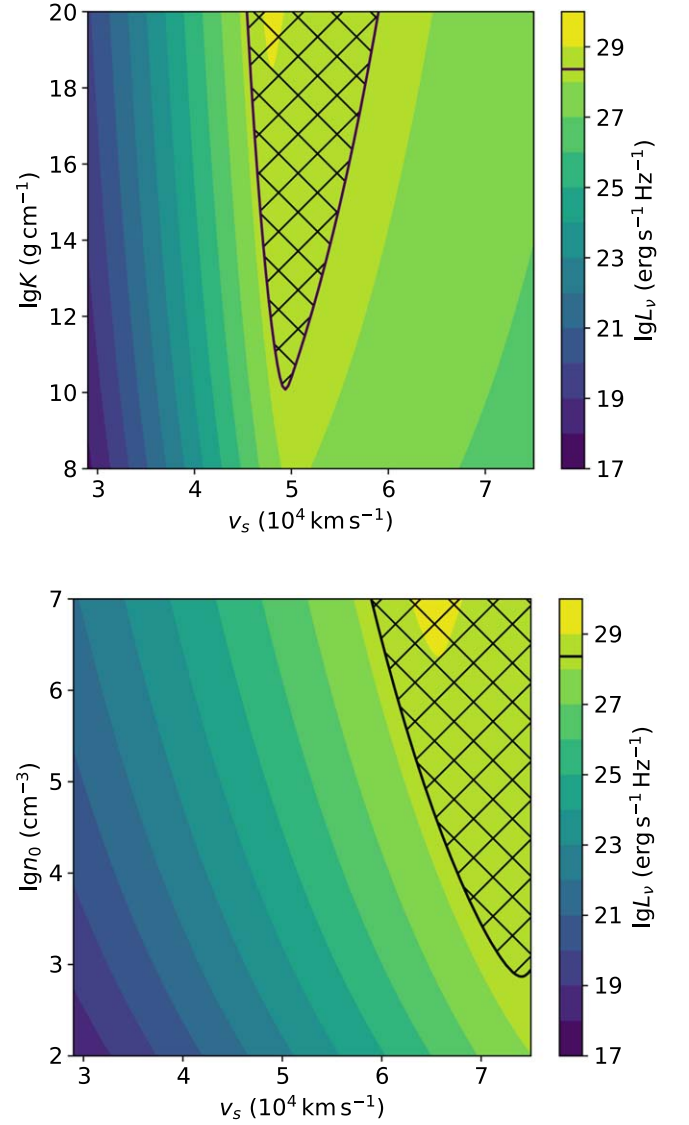


Figure B7. Maps of expected radio luminosity at 230 GHz. The x -axis is the shock velocity v_s . The y -axis is wind mass-loss parameter K in the case of $\rho \propto r^{-2}$ CSM environment in the upper panel, while in the bottom panel it is the number density n_0 in the constant-density case. The black contour in each panel shows the location of 3σ upper limit at 230 GHz on SN2019dge. The phase space with a luminosity higher than the black line in each panel is ruled out by the observation.

luminosity higher than the 3σ limits (indicated by the hatched regions), and thus our observations are not deep enough to provide stringent constraints on the circumstellar properties. Compared with 230 GHz, the parameter space is even more poorly constrained at 350 GHz and are thus not shown.

Appendix C Host-galaxy Properties

To obtain archival photometry of the host galaxy, we retrieve images from the Sloan Digital Sky Survey data release (DR9) (SDSS; Ahn et al. 2012), the Panoramic Survey Telescope and Rapid Response System (Pan-STARRS, PS1), DR1 (Flewelling et al. 2016), the Two Micron All Sky Survey (2MASS; Skrutskie et al. 2006), and the unWISE images (Lang 2014) from the NEOWISE Reactivation Year-3 (Meisner et al. 2017). We augment this data set with Swift/UVOT observations that extend our wavelength coverage to the UV. The photometry is extracted with the software package LAMBDA (Lambda Adaptive Multiband Deblending Algorithm in R; Wright et al. 2016), to perform consistent photometry on images that are neither pixel nor seeing matched, and tools presented in S. Schulze et al. (2020, in preparation). The UVOT data are reduced in HEASOFT as described in Section 2.2.3. The measured host photometry is given in Table C1.

We measure properties of the host galaxy using the spectrum obtained at phase +314.4 days, assuming that the most prominent nebular line emissions of H α and [N II] are from the host. The Galactic extinction corrected emission line fluxes of H α and [N II] λ 6584 are $(24.15 \pm 0.54) \times 10^{-16}$ erg cm $^{-2}$ s $^{-1}$ and $(1.92 \pm 0.10) \times 10^{-16}$ erg cm $^{-2}$ s $^{-1}$, respectively. The fluxes were measured by fitting a Gaussian profile to the emission line profiles, measuring the integrated flux under the profile.

Using the Kennicutt (1998) relation converted to a Chabrier initial mass function (Chabrier 2003; Madau & Dickinson 2014), we infer a star formation rate of $\approx 0.012 M_{\odot} \text{yr}^{-1}$ from the H α emission line. Note that this is a lower limit because the slit width in the LRIS spectrum is 1''0 (~ 0.44 kpc at the distance of the host) and the extraction aperture is 0''76, whereas the host diameter is about 4''.

We also compute the oxygen abundance using the strong-line metallicity indicator N2 23 (Pettini & Pagel 2004) with the updated calibration reported in Marino et al. (2013). The oxygen abundance in the N2 scale is 8.23 ± 0.01 (stat) ± 0.05 (sys). We choose not to use the O3N2 index 24 because it requires line flux measurement of H β . As can be seen in panel (a) Figure 10, there is substantial stellar absorption around H β (4861 Å). Compared with $12 + \log(\text{O}/\text{H})_{\text{solar}} = 8.69$ (Asplund et al. 2009), the derived N2 index suggests a significantly subsolar metallicity of $\approx 0.35 Z_{\odot}$ ($Z \approx 0.005$). This estimate places SN2019dge's host galaxy in the lowest 10% of the distribution of SNe Ibc host-galaxy metallicities (Sanders et al. 2012), and it is on the lowest 15% in the range of Type Icb host-galaxy metallicities (Modjaz et al. 2020).

We determine the stellar mass (M_{\star}) of the host galaxy by SED modeling using CIGALE (Boquien et al. 2019). We adopt the stellar population synthesis models from Bruzual & Charlot (2003) with the Kroupa initial mass function (IMF) (Kroupa 2001), and assume a double declining exponential star formation history (SFH). In addition, a dust component is added using the Draine & Li (2007) model to account for dust emission. Finally, the total SED model is attenuated by a modified Calzetti extinction law (Calzetti et al. 2000). It assumes that the young stellar population is extinguished by the normal Calzetti law, and the old stellar population is extinguished

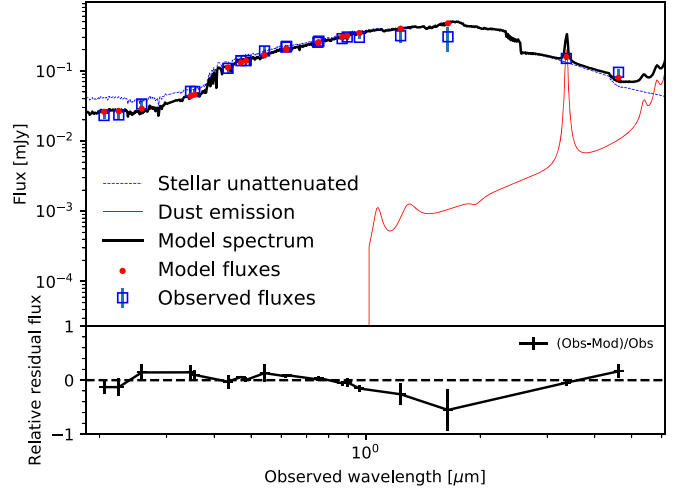


Figure C1. Spectral energy distribution of the host galaxy of SN2019dge. The observed photometric data (with 1σ error bars) are shown in blue open squares, and the model is shown as a black curve (reduced $\chi^2 = 0.64$). The relative residual flux is shown in the bottom panel.

Table C1
Photometry of the Host Galaxy

Instrument/Filter	λ_{eff} (Å)	m	σ_m
UVOT/UVW2	2079.0	20.492	0.124
UVOT/UVW2	2255.1	20.471	0.172
UVOT/UVW1	2614.2	20.081	0.155
UVOT/U	3475.5	19.631	0.145
UVOT/B	4359.1	18.812	0.139
UVOT/V	5430.1	18.194	0.171
SDSS/u'	3561.8	19.636	0.082
SDSS/g'	4718.9	18.540	0.015
SDSS/r'	6185.2	18.056	0.026
SDSS/i'	7499.7	17.885	0.028
SDSS/z'	8961.5	17.697	0.089
PS1/g _{PS1}	4866.5	18.538	0.042
PS1/r _{PS1}	6214.6	18.029	0.030
PS1/i _{PS1}	7544.6	17.845	0.033
PS1/z _{PS1}	8679.5	17.755	0.050
PS1/y _{PS1}	9633.3	17.710	0.063
2MASS/J	12410.5	17.653	0.215
2MASS/H	16513.7	17.690	0.420
WISE/W1	34002.6	18.460	0.069
WISE/W2	46520.1	18.953	0.136

Note. m and σ_m are observed magnitude (without extinction correction) in the AB system.


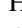






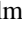

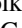

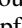


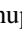



less heavily than that by a certain factor (< 1 , Charlot & Fall 2000).

The fitted SED is shown in Figure C1. The derived total stellar mass is $\log(M_{\star, \text{tot}}/M_{\odot}) = 8.5 \pm 0.1$, the mass of the stars alive is $\log(M_{\star, \text{alive}}/M_{\odot}) = 8.4 \pm 0.1$, and the inferred SFR is $0.030 \pm 0.005 M_{\odot} \text{yr}^{-1}$, about 2.5 times the SFR inferred from the H α flux measurement. The host extinction, $E(B - V)$, is 0.07 ± 0.02 mag and 0.03 ± 0.01 mag for the young and old stellar population, respectively, both of which are insignificant. The stellar mass and the SFR of the galaxy are in the lower half of the hosts of Type Ibc SN in the PTF sample (S. Schulze et al. 2020, in preparation).

23 $\text{N2} \equiv \log\{([\text{N II}] \lambda 6583/\text{H}\alpha)\}$.

24 $\text{O3N2} \equiv \log\{([\text{O III}] \lambda 5007/\text{H}\beta)/([\text{N II}] \lambda 6583/\text{H}\alpha)\}$.

ORCID iDs

Yuhan Yao  <https://orcid.org/0000-0001-6747-8509>
 Kishalay De  <https://orcid.org/0000-0002-8989-0542>
 Mansi M. Kasliwal  <https://orcid.org/0000-0002-5619-4938>
 Anna Y. Q. Ho  <https://orcid.org/0000-0002-9017-3567>
 Steve Schulze  <https://orcid.org/0000-0001-6797-1889>
 Zhihui Li  <https://orcid.org/0000-0001-5113-7558>
 S. R. Kulkarni  <https://orcid.org/0000-0001-5390-8563>
 Andrew Fruchter  <https://orcid.org/0000-0002-6652-9279>
 David Rubin  <https://orcid.org/0000-0001-5402-4647>
 Daniel A. Perley  <https://orcid.org/0000-0001-8472-1996>
 Jim Fuller  <https://orcid.org/0000-0002-4544-0750>
 Anthony L. Piro  <https://orcid.org/0000-0001-6806-0673>
 C. Fremling  <https://orcid.org/0000-0002-4223-103X>
 Eric C. Bellm  <https://orcid.org/0000-0001-8018-5348>
 Dmitry A. Duev  <https://orcid.org/0000-0001-5060-8733>
 Avishay Gal-Yam  <https://orcid.org/0000-0002-3653-5598>
 V. Zach Golkhou  <https://orcid.org/0000-0001-8205-2506>
 Matthew J. Graham  <https://orcid.org/0000-0002-3168-0139>
 George Helou  <https://orcid.org/0000-0003-3367-3415>
 Thomas Kupfer  <https://orcid.org/0000-0002-6540-1484>
 Russ R. Laher  <https://orcid.org/0000-0003-2451-5482>
 Frank J. Masci  <https://orcid.org/0000-0002-8532-9395>
 Adam A. Miller  <https://orcid.org/0000-0001-9515-478X>
 Ben Rusholme  <https://orcid.org/0000-0001-7648-4142>
 David L. Shupe  <https://orcid.org/0000-0003-4401-0430>
 Roger Smith  <https://orcid.org/0000-0001-7062-9726>
 Jesper Sollerman  <https://orcid.org/0000-0003-1546-6615>
 Maayane T. Soumagnac  <https://orcid.org/0000-0001-6753-1488>

References

- Abbott, B. P., Abbott, R., Abbott, T. D., et al. 2017a, *PhRvL*, **119**, 161101
 Abbott, B. P., Abbott, R., Abbott, T. D., et al. 2017b, *ApJL*, **848**, L12
 Abbott, B. P., Abbott, R., Abbott, T. D., et al. 2020, *ApJL*, **892**, L3
 Ahn, C. P., Alexandroff, R., Allende Prieto, C., et al. 2012, *ApJS*, **203**, 21
 Alam, S., Albareti, F. D., Allende Prieto, C., et al. 2015, *ApJS*, **219**, 12
 Andrews, J. J., & Mandel, I. 2019, *ApJL*, **880**, L8
 Arnett, W. D. 1982, *ApJ*, **253**, 785
 Asplund, M., Grevesse, N., Sauval, A. J., & Scott, P. 2009, *ARA&A*, **47**, 481
 Astropy Collaboration, Robitaille, T. P., Tollerud, E. J., et al. 2013, *A&A*, **558**, A33
 Barbary, K., Barclay, T., Biswas, R., et al. 2016, SNCosmo: Python Library for Supernova Cosmology v2.0, Astrophysics Source Code Library, ascl:1611.017
 Barnsley, R. M., Smith, R. J., & Steele, I. A. 2012, *AN*, **333**, 101
 Bellm, E. C., Kulkarni, S. R., Barlow, T., et al. 2019a, *PASP*, **131**, 068003
 Bellm, E. C., Kulkarni, S. R., Graham, M. J., et al. 2019b, *PASP*, **131**, 018002
 Bellm, E. C., & Sesar, B. 2016, pyraf-dbsp: Reduction Pipeline for the Palomar Double Beam Spectrograph v1.0, Astrophysics Source Code Library, ascl:1602.002
 Beniamini, P., & Piran, T. 2016, *MNRAS*, **456**, 4089
 Boquien, M., Burgarella, D., Roehly, Y., et al. 2019, *A&A*, **622**, A103
 Bruzual, G., & Charlot, S. 2003, *MNRAS*, **344**, 1000
 Bufano, F., Immler, S., Turatto, M., et al. 2009, *ApJ*, **700**, 1456
 Burrows, D. N., Hill, J. E., Nousek, J. A., et al. 2005, *SSRv*, **120**, 165
 Calzetti, D., Armus, L., Bohlin, R. C., et al. 2000, *ApJ*, **533**, 682
 Cardelli, J. A., Clayton, G. C., & Mathis, J. S. 1989, *ApJ*, **345**, 245
 Chabrier, G. 2003, *PASP*, **115**, 763
 Charlot, S., & Fall, S. M. 2000, *ApJ*, **539**, 718
 Chen, P., Dong, S., Stritzinger, M. D., et al. 2020, *ApJL*, **889**, L6
 Chevalier, R. A. 1982, *ApJ*, **259**, 302
 Chevalier, R. A. 1998, *ApJ*, **499**, 810
 Chugai, N. N., & Danziger, I. J. 1994, *MNRAS*, **268**, 173
 Coulter, D. A., Foley, R. J., Kilpatrick, C. D., et al. 2017, *Sci*, **358**, 1556
 De, K., Hankins, M. J., Kasliwal, M. M., et al. 2020a, *PASP*, **132**, 025001
 De, K., Kasliwal, M. M., Cantwell, T., et al. 2018b, *ApJ*, **866**, 72
 De, K., Kasliwal, M. M., Ofek, E. O., et al. 2018c, *Sci*, **362**, 201
 De, K., Kasliwal, M. M., Tzanidakis, A., et al. 2020a, arXiv:2004.09029
 Dekany, R., Smith, R. M., Riddle, R., et al. 2020, *PASP*, **132**, 038001
 Dessart, L., Hillier, D. J., Li, C., & Woosley, S. 2012, *MNRAS*, **424**, 2139
 Dey, A., Schlegel, D. J., Lang, D., et al. 2019, *AJ*, **157**, 168
 Draine, B. T., & Li, A. 2007, *ApJ*, **657**, 810
 Drout, M. R., Soderberg, A. M., Gal-Yam, A., et al. 2011, *ApJ*, **741**, 97
 Drout, M. R., Soderberg, A. M., Mazzali, P. A., et al. 2013, *ApJ*, **774**, 58
 East, W. E., & Pretorius, F. 2012, *ApJL*, **760**, L4
 Eldridge, J. J., Fraser, M., Smartt, S. J., et al. 2013, *MNRAS*, **436**, 774
 Feindt, U., Nordin, J., Rigault, M., et al. 2019, *JCAP*, **2019**, 005
 Filippenko, A. V. 1997, *ARA&A*, **35**, 309
 Flewelling, H. A., Magnier, E. A., Chambers, K. C., et al. 2016, arXiv:1612.05243
 Foreman-Mackey, D. 2016, *JOSS*, **1**, 24
 Foreman-Mackey, D., Hogg, D. W., Lang, D., & Goodman, J. 2013, *PASP*, **125**, 306
 Fransson, C., Benvenuti, P., Gordon, C., et al. 1984, *A&A*, **132**, 1
 Fremling, C., Ko, H., Dugas, A., et al. 2019, *ApJL*, **878**, L5
 Fremling, C., Sollerman, J., Kasliwal, M. M., et al. 2018, *A&A*, **618**, A37
 Fremling, C., Sollerman, J., Taddia, F., et al. 2016, *A&A*, **593**, A68
 Fremling, U. C., Miller, A. A., Sharma, Y., et al. 2020, *ApJ*, **895**, 32
 Gal-Yam, A. 2017, in *Handbook of Supernovae*, ed. A. W. Alsabti & P. Murdin (Berlin: Springer), 195
 Gal-Yam, A., Arcavi, I., Ofek, E. O., et al. 2014, *Natur*, **509**, 471
 Gal-Yam, A., Bufano, F., Barlow, T. A., et al. 2008, *ApJL*, **685**, L117
 Gehrels, N., Chincarini, G., Giommi, P., et al. 2004, *ApJ*, **611**, 1005
 Goldstein, A., Veres, P., Burns, E., et al. 2017, *ApJL*, **848**, L14
 Graham, M. J., Kulkarni, S. R., Bellm, E. C., et al. 2019, *PASP*, **131**, 078001
 Guillochon, J., Parent, J., Kelley, L. Z., & Margutti, R. 2017, *ApJ*, **835**, 64
 Hachinger, S., Mazzali, P. A., Taubenberger, S., et al. 2012, *MNRAS*, **422**, 70
 Hallinan, G., Corsi, A., Mooley, K. P., et al. 2017, *Sci*, **358**, 1579
 Hamuy, M., Maza, J., Pinto, P. A., et al. 2002, *AJ*, **124**, 417
 HEASARC 2014, HEASoft: Unified Release of FTOOLS and XANADU v.6.17, Astrophysics Source Code Library, ascl:1408.004
 Hijikawa, K., Kinugawa, T., Yoshida, T., & Umeda, H. 2019, *ApJ*, **882**, 93
 Ho, A. Y. Q., Goldstein, D. A., Schulze, S., et al. 2019a, *ApJ*, **887**, 169
 Ho, A. Y. Q., Perley, D. A., Beniamini, P., et al. 2020a, arXiv:2006.10761
 Ho, A. Y. Q., Perley, D. A., Kulkarni, S. R., et al. 2020b, *ApJ*, **895**, 49
 Ho, A. Y. Q., Phinney, E. S., Ravi, V., et al. 2019b, *ApJ*, **871**, 73
 Ho, P. T. P., Moran, J. M., & Lo, K. Y. 2004, *ApJL*, **616**, L1
 Horesh, A., Stockdale, C., Fox, D. B., et al. 2013, *MNRAS*, **436**, 1258
 Hosseinzadeh, G., Arcavi, I., Valenti, S., et al. 2017, *ApJ*, **836**, 158
 Huang, C., & Chevalier, R. A. 2018, *MNRAS*, **475**, 1261
 Hunter, J. D. 2007, *CSE*, **9**, 90
 Jacobson-Galán, W. V., Foley, R. J., Schwab, J., et al. 2019, *MNRAS*, **487**, G58
 Jacobson-Galán, W. V., Margutti, R., Kilpatrick, C. D., et al. 2020, *ApJ*, **898**, 166
 Jeffery, D. J., Kirshner, R. P., Challis, P. M., et al. 1994, *ApJL*, **421**, L27
 Jeffreys, H. 1946, *RSPSA*, **186**, 453
 Kasen, D. 2017, in *Handbook of Supernovae*, ed. A. W. Alsabti & P. Murdin (Berlin: Springer), 939
 Kasliwal, M. M., Cannella, C., Bagdasaryan, A., et al. 2019, *PASP*, **131**, 038003
 Kasliwal, M. M., Kulkarni, S. R., Gal-Yam, A., et al. 2010, *ApJL*, **723**, L98
 Kasliwal, M. M., Kulkarni, S. R., Gal-Yam, A., et al. 2012, *ApJ*, **755**, 161
 Kasliwal, M. M., Nakar, E., Singer, L. P., et al. 2017, *Sci*, **358**, 1559
 Kennicutt, Robert C. J. 1998, *ApJ*, **498**, 541
 Khatami, D. K., & Kasen, D. N. 2019, *ApJ*, **878**, 56
 Khazov, D., Yaron, O., Gal-Yam, A., et al. 2016, *ApJ*, **818**, 3
 Kingdon, J., Ferland, G. J., & Feibelman, W. A. 1995, *ApJ*, **439**, 793
 Kleiser, I., Fuller, J., & Kasen, D. 2018a, *MNRAS*, **481**, L141
 Kleiser, I. K. W., & Kasen, D. 2014, *MNRAS*, **438**, 318
 Kleiser, I. K. W., Kasen, D., & Duffell, P. C. 2018b, *MNRAS*, **475**, 3152
 Komatsu, E., Smith, K. M., Dunkley, J., et al. 2011, *ApJS*, **192**, 18
 Krupa, P. 2001, *MNRAS*, **322**, 231
 Lang, D. 2014, *AJ*, **147**, 108
 Laplace, E., Göteborg, Y., de Mink, S. E., et al. 2020, *A&A*, **637**, 6
 Law, N. M., Kulkarni, S. R., Dekany, R. G., et al. 2009, *PASP*, **121**, 1395
 Leibundgut, B., Kirshner, R. P., Pinto, P. A., et al. 1991, *ApJ*, **372**, 531
 Li, H., & McCray, R. 1992, *ApJ*, **387**, 309
 Li, W., Chornock, R., Leaman, J., et al. 2011a, *MNRAS*, **412**, 1473
 Li, W., Leaman, J., Chornock, R., et al. 2011b, *MNRAS*, **412**, 1441

- Liu, Y.-Q., Modjaz, M., Bianco, F. B., & Graur, O. 2016, *ApJ*, **827**, 90
- Luridiana, V., Morisset, C., & Shaw, R. A. 2015, *A&A*, **573**, 42
- Lyman, J. D., Bersier, D., James, P. A., et al. 2016, *MNRAS*, **457**, 328
- Madau, P., & Dickinson, M. 2014, *ARA&A*, **52**, 415
- Margutti, R., Metzger, B. D., Chornock, R., et al. 2019, *ApJ*, **872**, 18
- Marino, R. A., Rosales-Ortega, F. F., Sánchez, S. F., et al. 2013, *A&A*, **559**, A114
- Masci, F. J., Laher, R. R., Rusholme, B., et al. 2019, *PASP*, **131**, 018003
- Mazzali, P. A., Sullivan, M., Hachinger, S., et al. 2014, *MNRAS*, **439**, 1959
- McBrien, O. R., Smartt, S. J., Chen, T.-W., et al. 2019, *ApJL*, **885**, L23
- McKinney, W. 2010, in Proc. 9th Python in Science Conference (SciPy 2010), Data Structures for Statistical Computing in Python, ed. S. van der Walt & J. Millman (Trieste: SISSA), 56
- Meisner, A. M., Lang, D., & Schlegel, D. J. 2017, *AJ*, **153**, 38
- Miller, A. A., Yao, Y., Bulla, M., et al. 2020, arXiv:2001.00598
- Modjaz, M., Bianco, F. B., Siwek, M., et al. 2020, *ApJ*, **892**, 153
- Modjaz, M., Gutiérrez, C. P., & Arcavi, I. 2019, *NatAs*, **3**, 717
- Moriya, T., Tominaga, N., Tanaka, M., et al. 2010, *ApJ*, **719**, 1445
- Moriya, T. J., Mazzali, P. A., Tominaga, N., et al. 2017, *MNRAS*, **466**, 2085
- Moriya, T. J., Tominaga, N., Langer, N., et al. 2014, *A&A*, **569**, A57
- Nadyozhin, D. K. 1994, *ApJS*, **92**, 527
- Nakaoka, T., Maeda, K., Yamanaka, M., et al. 2020, arXiv:2005.02992
- Nakar, E., & Piro, A. L. 2014, *ApJ*, **788**, 193
- Nomoto, K., Yamaoka, H., Pols, O. R., et al. 1994, *Natur*, **371**, 227
- Ofek, E. O., Fox, D., Cenko, S. B., et al. 2013a, *ApJ*, **763**, 42
- Ofek, E. O., Lin, L., Kouveliotou, C., et al. 2013b, *ApJ*, **768**, 47
- Oke, J. B., Cohen, J. G., Carr, M., et al. 1995, *PASP*, **107**, 375
- Oke, J. B., & Gunn, J. E. 1982, *PASP*, **94**, 586
- Panagia, N., Vettolani, G., Boksenberg, A., et al. 1980, *MNRAS*, **192**, 861
- Pastorello, A., Benetti, S., Brown, P. J., et al. 2015, *MNRAS*, **449**, 1921
- Pastorello, A., Mattila, S., Zampieri, L., et al. 2008, *MNRAS*, **389**, 113
- Patterson, M. T., Bellm, E. C., Rusholme, B., et al. 2019, *PASP*, **131**, 018001
- Peimbert, M., Peimbert, A., & Delgado-Inglada, G. 2017, *PASP*, **129**, 082001
- Peimbert, M., Peimbert, A., & Ruiz, M. T. 2000, *ApJ*, **541**, 688
- Perley, D. A. 2019, *PASP*, **131**, 084503
- Perley, D. A., Mazzali, P. A., Yan, L., et al. 2019, *MNRAS*, **484**, 1031
- Pettini, M., & Pagel, B. E. J. 2004, *MNRAS*, **348**, L59
- Piascik, A. S., Steele, I. A., Bates, S. D., et al. 2014, *Proc. SPIE*, **9147**, 91478H
- Piran, T., & Shaviv, N. J. 2005, *PhRvL*, **94**, 051102
- Piro, A. L. 2015, *ApJL*, **808**, L51
- Piro, A. L., Haynie, A., & Yao, Y. 2020, arXiv:2007.08543
- Piro, A. L., & Morozova, V. S. 2014, *ApJL*, **792**, L11
- Polin, A., Nugent, P., & Kasen, D. 2019, *ApJ*, **873**, 84
- Poznanski, D., Chornock, R., Nugent, P. E., et al. 2010, *Sci*, **327**, 58
- Prentice, S. J., Ashall, C., James, P. A., et al. 2019, *MNRAS*, **485**, 1559
- Prentice, S. J., Maguire, K., Smartt, S. J., et al. 2018, *ApJL*, **865**, L3
- Quataert, E., & Shiode, J. 2012, *MNRAS*, **423**, L92
- Rasmussen, C. E., & Williams, C. K. I. 2003, Gaussian Processes for Machine Learning (Cambridge, MA: MIT Press), 63
- Rau, A., Kulkarni, S. R., Law, N. M., et al. 2009, *PASP*, **121**, 1334
- Rest, A., Garnavich, P. M., Khatami, D., et al. 2018, *NatAs*, **2**, 307
- Rigault, M. 2018, ztfquery, a python tool to access ZTF data, Zenodo doi:10.5281/zenodo.1345222
- Roming, P. W. A., Kennedy, T. E., Mason, K. O., et al. 2005, *SSRv*, **120**, 95
- Sanders, N. E., Soderberg, A. M., Levesque, E. M., et al. 2012, *ApJ*, **758**, 132
- Schlafly, E. F., & Finkbeiner, D. P. 2011, *ApJ*, **737**, 103
- Shen, K. J., Kasen, D., Weinberg, N. N., et al. 2010, *ApJ*, **715**, 767
- Shivvers, I., Filippenko, A. V., Silverman, J. M., et al. 2019, *MNRAS*, **482**, 1545
- Shivvers, I., Zheng, W., Van Dyk, S. D., et al. 2017, *MNRAS*, **471**, 4381
- Sim, S. A., Fink, M., Kromer, M., et al. 2012, *MNRAS*, **420**, 3003
- Skrutskie, M. F., Cutri, R. M., Stiening, R., et al. 2006, *AJ*, **131**, 1163
- Smith, N. 2014, *ARA&A*, **52**, 487
- Smith, N. 2017, in Handbook of Supernovae, ed. A. W. Alsabti & P. Murdin (Berlin: Springer), 403
- Smith, N., Li, W., Filippenko, A. V., & Chornock, R. 2011, *MNRAS*, **412**, 1522
- Smith, N., Mauerhan, J. C., Cenko, S. B., et al. 2015, *MNRAS*, **449**, 1876
- Steele, I. A., Smith, R. J., Rees, P. C., et al. 2004, *Proc. SPIE*, **5489**, 679
- Storey, P. J., & Hummer, D. G. 1995, *MNRAS*, **272**, 41
- Sullivan, M., Kasliwal, M. M., Nugent, P. E., et al. 2011, *ApJ*, **732**, 118
- Suwa, Y., Yoshida, T., Shibata, M., et al. 2015, *MNRAS*, **454**, 3073
- Taddia, F., Stritzinger, M. D., Bersten, M., et al. 2018, *A&A*, **609**, A136
- Tauris, T. M., Kramer, M., Freire, P. C. C., et al. 2017, *ApJ*, **846**, 170
- Tauris, T. M., Langer, N., Moriya, T. J., et al. 2013, *ApJL*, **778**, L23
- Tauris, T. M., Langer, N., & Podsiadlowski, P. 2015, *MNRAS*, **451**, 2123
- Valenti, S., Benetti, S., Cappellaro, E., et al. 2008, *MNRAS*, **383**, 1485
- Virtanen, P., Gommers, R., Oliphant, T. E., et al. 2020, *NatMe*, **17**, 261
- Weiler, K. W., Williams, C. L., Panagia, N., et al. 2007, *ApJ*, **671**, 1959
- Wellons, S., Soderberg, A. M., & Chevalier, R. A. 2012, *ApJ*, **752**, 17
- Wheeler, J. C., Johnson, V., & Clocchiatti, A. 2015, *MNRAS*, **450**, 1295
- Whitesides, L., Lunnan, R., Kasliwal, M. M., et al. 2017, *ApJ*, **851**, 107
- Willingale, R., Starling, R. L. C., Beardmore, A. P., et al. 2013, *MNRAS*, **431**, 394
- Woosley, S. E. 2019, *ApJ*, **878**, 49
- Wright, A. H., Robotham, A. S. G., Bourne, N., et al. 2016, *MNRAS*, **460**, 765
- Wygoda, N., Elbaz, Y., & Katz, B. 2019, *MNRAS*, **484**, 3951
- Yan, L., Quimby, R., Gal-Yam, A., et al. 2017, *ApJ*, **840**, 57
- Yao, Y., Miller, A. A., Kulkarni, S. R., et al. 2019, *ApJ*, **886**, 152
- Yaron, O., & Gal-Yam, A. 2012, *PASP*, **124**, 668
- Yaron, O., Perley, D. A., Gal-Yam, A., et al. 2017, *NatPh*, **13**, 510
- Yoon, S. C., Woosley, S. E., & Langer, N. 2010, *ApJ*, **725**, 940
- Zackay, B., Ofek, E. O., & Gal-Yam, A. 2016, *ApJ*, **830**, 27
- Zapartas, E., de Mink, S. E., Van Dyk, S. D., et al. 2017, *ApJ*, **842**, 125